

STUDY OF BEAM-HALO EVENTS IN PHOTON PRODUCTION IN THE CMS
EXPERIMENT

A THESIS SUBMITTED TO
THE GRADUATE SCHOOL OF NATURAL AND APPLIED SCIENCES
OF
MIDDLE EAST TECHNICAL UNIVERSITY

BY

EDA YILDIRIM

IN PARTIAL FULFILLMENT OF THE REQUIREMENTS
FOR
THE DEGREE OF MASTER OF SCIENCE
IN
PHYSICS

SEPTEMBER 2011

Approval of the thesis:

**STUDY OF BEAM-HALO EVENTS IN PHOTON PRODUCTION IN THE CMS
EXPERIMENT**

submitted by **EDA YILDIRIM** in partial fulfillment of the requirements for the degree of
Master of Science in Physics Department, Middle East Technical University by,

Prof. Dr. Canan Özgen
Dean, Graduate School of **Natural and Applied Sciences**

Prof. Dr. Sinan Bilikmen
Head of Department, **Physics**

Prof. Dr. Ali Murat Güler
Supervisor, **Physics Department, METU**

Examining Committee Members:

Prof. Dr. Ramazan Sever
Physics Department, METU

Prof. Dr. Ali Murat Güler
Physics Department, METU

Prof. Dr. Atalay Karasu
Physics Department, METU

Prof. Dr. Bayram Tekin
Physics Department, METU

Assoc. Prof. Korkut Okan Ozansoy
Physics Engineering Department, Ankara University

Date:

I hereby declare that all information in this document has been obtained and presented in accordance with academic rules and ethical conduct. I also declare that, as required by these rules and conduct, I have fully cited and referenced all material and results that are not original to this work.

Name, Last Name: EDA YILDIRIM

Signature :

ABSTRACT

STUDY OF BEAM-HALO EVENTS IN PHOTON PRODUCTION IN THE CMS EXPERIMENT

Yıldırım, Eda

M.Sc., Department of Physics

Supervisor : Prof. Dr. Ali Murat Güler

September 2011, 56 pages

The Compact Muon Solenoid (CMS) Experiment operates at the Large Hadron Collider (LHC) which is the highest energy particle accelerator in the world. CMS is a general purpose detector designed to investigate a wide range of physics, including the search for the Higgs boson. The measurement of photon production in the CMS experiment is crucial since it represents an irreducible background for many new physics searches, such as decay of Higgs to two photon, supersymmetry and extra-dimensions. The study of beam halo contamination is important for the correct measurement of photon production. This thesis presents a way to identify and remove this contamination by using the timing and the shower shape of the photons.

Keywords: CERN, CMS, photon, beam-halo, 2010 data

ÖZ

CMS DENEYİNDEKİ FOTON ÜRETİMİNDE DEMET-HALE OLAYLARININ ÇALIŞILMASI

Yıldırım, Eda

Yüksek Lisans, Fizik Bölümü

Tez Yöneticisi : Prof. Dr. Ali Murat Güler

Eylül 2011, 56 sayfa

Compact Muon Solenoid (CMS) deneyi, dünyanın en yüksek enerjili parçacık hızlandırıcısı olan Büyük Hadron Çarpıştırıcısında (BHÇ) yer almaktadır. Genel amaçlı CMS deneyi, Higgs bozonu arařtırmaları da dahil olmak üzere geniş çapta fizik arařtırmaları yapılmak üzere tasarlanmıřtır. CMS deneyinde foton üretimi ölçümleri, Higgs'in iki fotona bozulumu, süpersimetri ve ekstra-boyutlar gibi birçok yeni fizik arařtırmalarının kaçınılmaz arka planı olduđu için önemli bir yere sahiptir. Demet-hale kirliliđi çalışmaları ise foton üretimi ölçümlerinin dođru yapılabilmesi için önemlidir. Bu tezde demet-hale kirliliđinin, fotonların zamanlamasını ve saçılım şeklini kullanarak belirlenip yok edilmesi için bir yöntem sunulmuřtur.

Anahtar Kelimeler: CERN, CMS, foton, demet-hale, 2010 data

To Totinim

ACKNOWLEDGMENTS

It is a pleasure to thank those who helped and supported me during the preparation of this thesis, during my education and life.

First of all, I would like to thank to my supervisor Prof. Dr. Ali Murat Güler for getting me involved in the CMS Collaboration, without this opportunity this thesis would not have been possible.

I would like to thank to the members of the QCD Photons group of the CMS Collaboration. In particular, to Dr. Darko Mekterovic, Dr. Syue-Wei Li and Kadir Öcalan for their helps and advices. Despite their busy schedule, they always tried to allocate some time for me. Especially, I am indebted to my colleague Kadir Öcalan for his moral support and guidance.

I owe my deepest gratitude to Prof. Dr. Ayşe Kalkanlı Karasu whom I call “my academic mother”. Ever since I started my undergraduate, she listened and guided me in every problem I faced. I was so lucky that I had her as my academic advisor.

My special thanks go to my grandmother, Totinim, to whom this thesis is dedicated. She has been a great grandmother, mother and friend. She was always there for me to listen and to give advices. Hearing her voice was enough to cheer up. I am grateful to my family for their support in every aspect. My father, Mustafa, always worked hard to provide us a better future. He taught me to be moral and idealist. My mother, Yasemin, did everything in her power to make us happy. She taught me to be honest and strong. My sister, Yeldağ, has been always a good sister. Her experiences and advices about the university life were always a useful guidance. My brother, Yarkın, has been a good friend of mine that I could count on. He helped me whenever I needed him. My cousin, Büşra, has been one of my best friends. I could never forget the holidays we spent together. They all believed in me and supported me in every decision I made. I am proud of each one of them and I feel so lucky to be a member of this family.

I would like to express my profound gratitudes to my dear friend Özlem Kaya for her support

in every manner. She is more than just a friend to me. I could never get how she could understand me so well. She helped me get through many difficulties. She is the only one that I could actually believe when she says “everything’s gonna be okay”. She and her daughter, Nisan, are the source of cheer and fun. I am so glad that I got the opportunity to know them.

I wish to thank Tuğba Kaya and Tansel Deniz for their sincere and precious friendship. They have been there for me in both good and bad days for the past 5 years. They have been like family to me in Ankara.

The most fun moments during the preparation of this thesis was the coffee breaks that I had with Buğra Bilin, Bora Işıldak and Özlem Kaya, which I enjoyed every second of them. I would like to thank those people for that relaxing and precious times. Also, I owe a special thank to Buğra Bilin for coming up with the word “obtain” when I was stuck in the writing process.

I also would like to thank my friends for their friendship; Ceren Masatçı whom we grow up together, Zeynep Türkşen one of my best friends, Olgu Demircioğlu the fun guy, Gönül Ünal always a good friend, Özgür Altınok the cheer guy, Işıl Pınar Öngün a good friend from undergraduate years, Gülbahar Cebesoy whom we spent nights drinking coffee in front of the dorm window and chatting, Metin Yalvaç, Utku Can, Özlem Yavaş and Cemali Kılınç.

TABLE OF CONTENTS

ABSTRACT	iv
ÖZ	v
ACKNOWLEDGMENTS	vii
TABLE OF CONTENTS	ix
LIST OF TABLES	xi
LIST OF FIGURES	xii
CHAPTERS	
1 INTRODUCTION	1
2 THEORY	3
2.1 The Standard Model	3
2.2 Quantum Chromodynamics	6
2.3 Prompt Photon Production in Experiments	7
3 THE CMS EXPERIMENT	11
3.1 The Large Hadron Collider (LHC)	11
3.2 The CMS Detector	13
3.2.1 Coordinate Conventions	14
3.2.2 Inner Tracking System	14
3.2.2.1 Pixel Detector	15
3.2.2.2 Silicon Strip Tracker	15
3.2.3 Electromagnetic Calorimeter	16
3.2.3.1 Lead Tungstate Crystals	17
3.2.3.2 Photodetectors	17
3.2.3.3 Preshower Detector	19
3.2.4 Hadronic Calorimeter	19

	3.2.5	Muon System	20
	3.2.6	Superconducting Magnet	22
	3.3	Trigger System and Data Acquisition	22
4		ISOLATED PHOTON ANALYSIS	24
	4.1	Motivation	24
	4.2	Data and simulation samples	24
	4.3	Event Selection	26
	4.3.1	Trigger Selection	26
	4.3.2	Vertex Selection	27
	4.3.3	Photon Reconstruction	27
	4.3.3.1	Hybrid Algorithm	28
	4.3.3.2	Multi5 × 5 Algorithm	29
	4.3.3.3	Super-cluster Position Estimation	31
	4.3.3.4	Energy Corrections	31
	4.4	Photon Identification and Isolation	33
	4.5	Properties of Isolated Photons	34
	4.5.1	Efficiency of Photon Identification	34
	4.5.2	Shower Shapes of Isolated Photons	36
	4.6	Beam Halo Photons Removal	39
	4.6.1	Properties of Beam Halo Photons	39
	4.6.2	Cuts	44
	4.6.3	Efficiency of the Cuts	50
5		CONCLUSION	53
		REFERENCES	55

LIST OF TABLES

TABLES

Table 2.1	Quark classification	4
Table 2.2	Lepton classification	4
Table 2.3	The fundamental forces	5
Table 4.1	Summary of the data sets	25
Table 4.2	Summary of MC samples for signal used in the analysis	25
Table 4.3	Summary of MC samples for background used in the analysis	26
Table 4.4	Summary of HLT paths	27
Table 4.5	Usual values of the Hybrid clustering algorithm parameters	29
Table 4.6	Usual values of the Multi5 × 5 clustering algorithm parameters	31
Table 4.7	Isolation cuts	34
Table 4.8	Efficiency of photon identification	36
Table 4.9	Table of cuts that are used to remove beam halo photons	44
Table 4.10	Efficiency of the timing cut	51
Table 4.11	Efficiency of the $\sigma_{i\phi\phi}$ cut	52
Table 4.12	Efficiency of the rectangle cut	52
Table 4.13	Efficiency of the line cut	52

LIST OF FIGURES

FIGURES

Figure 2.1	Examples of Feynman diagrams	5
Figure 2.2	A strong interaction vertex	7
Figure 2.3	Gluon-gluon vertices	7
Figure 2.4	Feynman diagrams contributing to photon production	8
Figure 2.5	Measured differential isolated prompt photon cross section using the CMS Experiment	9
Figure 2.6	Measured differential isolated prompt photon cross section using the AT- LAS Experiment	10
Figure 3.1	The Large Hadron Collider	12
Figure 3.2	CERN Accelerator Complex	12
Figure 3.3	The CMS detector	13
Figure 3.4	The CMS detector layers	14
Figure 3.5	Geometrical layout of the pixel detector	15
Figure 3.6	Schematic cross section through the CMS tracker system	16
Figure 3.7	Transverse view of the electromagnetic calorimeter (ECAL)	17
Figure 3.8	Lead tungstate crystals with photodetectors attached	18
Figure 3.9	Longitudinal view of the hadron calorimeter	20
Figure 3.10	Longitudinal view of the muon system	21
Figure 3.11	Superconducting magnet of CMS	22
Figure 4.1	Illustration of Hybrid clustering algorithm	29
Figure 4.2	Illustration of Multi 5×5 clustering algorithm	30

Figure 4.3	Efficiency of photon identification	35
Figure 4.4	Super-cluster eta distribution of isolated photons	37
Figure 4.5	Super-cluster phi distribution of isolated photons	37
Figure 4.6	Distribution of the shower shape variable $\sigma_{i\eta\eta}$ of the isolated photons . . .	38
Figure 4.7	Distribution of the shower shape variable $\sigma_{i\phi\phi}$ of the isolated photons . . .	38
Figure 4.8	Shower shape in η -direction	40
Figure 4.9	Shower shape in different p_T bins	40
Figure 4.10	Arrival time of photons	41
Figure 4.11	Arrival time of photons that have $80 < p_T < 100$ GeV	41
Figure 4.12	$\sigma_{i\phi\phi}$ versus $\sigma_{i\eta\eta}$ for photons that have $80 < p_T < 100$ GeV and $ \eta_{SC} <$ 1.4442	42
Figure 4.13	t_{seed} versus $\sigma_{i\eta\eta}$ for photons that have $80 < p_T < 100$ GeV and $ \eta_{SC} <$ 1.4442	42
Figure 4.14	$\sigma_{i\phi\phi}$ versus t_{seed} for photons that have $80 < p_T < 100$ GeV and $ \eta_{SC} <$ 1.4442	43
Figure 4.15	$\sigma_{i\eta\eta}/\sigma_{i\phi\phi}$ versus t_{seed} for photons that have $80 < p_T < 100$ GeV and $ \eta_{SC} < 1.4442$	43
Figure 4.16	Timing cut on t_{seed} versus η_{SC} graph	44
Figure 4.17	Timing cut on t_{seed} versus $\sigma_{i\eta\eta}$ graph	45
Figure 4.18	$\sigma_{i\phi\phi}$ cut on $\sigma_{i\phi\phi}$ versus $\sigma_{i\eta\eta}$ graph	45
Figure 4.19	Rectangle cut on $\sigma_{i\phi\phi}$ versus t_{seed} graph	46
Figure 4.20	Line cut on $\sigma_{i\phi\phi}$ versus t_{seed} graph	46
Figure 4.21	Plots after applying the timing cut	47
Figure 4.22	Plots after applying the $\sigma_{i\phi\phi}$ cut	48
Figure 4.23	Plots after applying the rectangle cut	48
Figure 4.24	Plots after applying the line cut	49
Figure 4.25	$\sigma_{i\eta\eta}$ distributions after applying the cuts	49
Figure 4.26	Efficiency for the timing cut	50
Figure 4.27	Efficiency for the $\sigma_{i\phi\phi}$ cut	50

Figure 4.28 Efficiency for the rectangle cut	51
Figure 4.29 Efficiency for the line cut	51

CHAPTER 1

INTRODUCTION

CERN (Conseil Européen pour la Recherche Nucléaire), European Organization for Nuclear Research, is one of the largest research facilities of its type in the world. It is an international collaboration supported by many countries, both financially and intellectually. It is located in the Swiss-French border and its main function is to provide accelerated beams of particles that can be used for the experimental purposes. It develops and maintains particle accelerators, detectors and research facilities. Large Hadron Collider (LHC), the most powerful accelerator in the world with its design to reach beam energies up to 7 TeV, is the accelerator that operates at CERN nowadays. By the help of the detectors, the aim is to find new particles, testing the Standard Model of particle physics and beyond it.

The most popular research subject is the hunt for the Higgs particle which is predicted by the Standard Model yet not observed. There are many decay channels of the Higgs boson and one of them is to decay into two photons. For this channel, like every new physics channel that has photon in its final state, to be well understood, the studies of the photon production and identification are crucial. To get the precise measurement of photon production, its selection procedure has to be studied in order to distinguish it from its background events. One of these backgrounds is coming from the beam halo events. The subject of this thesis is the identification of the photons coming from the beam halo events and their removal. This thesis presents a way of achieving this goal using the shower shapes and the timing of the photons.

In Chapter 2, the theoretical background needed to understand this study is introduced. In this chapter first the basics of the Standard Model of particle physics and quantum chromodynamics (QCD) are mentioned, more details can be found in references [1, 2, 3, 4]. Then the results of the prompt photon production cross section measurements from the experiments; CMS and

ATLAS are presented. For further information about these measurements see reference [5] for CMS and [6] for ATLAS.

The data used in this thesis is taken with the CMS experiment that is located in LHC. In Chapter 3, some information about LHC is given and then the CMS experiment, with all its subdetectors and data taking procedure, is presented. More information about LHC and CMS can be found in references [7] and [8, 9, 10], respectively.

The photon production analysis is described in Chapter 4. First, the data that has been used in this study is introduced. Then, the photon selections, that have been applied to the data, in order to get the signal photons are discussed in detail and some characteristics of the selected photons are shown. The background contaminations, which are found out to be coming from the beam halo events, are seen in those selected photons. Hence, the characteristics of beam halo events are discussed. According to those characteristics, some cuts are developed and applied to the data in order to remove the contamination. Finally, using Monte Carlo samples the efficiencies of these cuts are calculated and presented.

In the last part, Chapter 5, the results of the cuts are discussed with their advantages and disadvantages. Also, in this chapter, further directions are given.

The study that is conducted in the content of this thesis was also presented in the internal note of CMS [11].

CHAPTER 2

THEORY

2.1 The Standard Model

The Standard Model of particle physics is the most precise and satisfying model, it has been tested by many experiments and became a well-tested physics theory. It explains the interaction between fundamental particles.

The fundamental particles, known today, are grouped in to two basic types called quarks and leptons that and are listed in Tables 2.1 and 2.2, respectively [12]. Both leptons and quarks have spin $1/2$. They are grouped in to pairs called generations according to their reaction to the fundamental forces. The particles in the first generation are the lightest and the most stable ones. The ones in the second generation are heavier and less stable compared to the first generation. The heaviest and most unstable particles make up the third generation [13, 14]. There are also anti-particles that correspond to each fundamental particle. An anti-particle has the same mass, but opposite electric charge and quantum numbers with its corresponding particle [1].

Hadrons are composite particles that are divided into two classes: baryons and mesons. Baryons are fermions (half-integer spin) which consist of three quarks whereas mesons are bosons (integer spin) which consist of one quark and one anti-quark [15].

Table 2.1: Quark classification. The charges are given in units of the proton charge which is 1.602×10^{-19} Coulomb.

Generation	Flavor	Symbol	Charge	Mass MeV/c^2
First	down	d	$-1/3$	4.1 – 5.7
	up	u	$2/3$	1.7 – 3.1
Second	strange	s	$-1/3$	80 – 130
	charm	c	$2/3$	1180 – 1340
Third	bottom	b	$-1/3$	4130 – 4850
	top	t	$2/3$	171400 – 174400

Table 2.2: Lepton classification. The charges are given in units of the proton charge.

Generation	Flavor	Symbol	Charge	Mass MeV/c^2
First	electron	e	-1	0.511
	e neutrino	ν_e	0	$< 2 \times 10^{-6}$
Second	muon	μ	-1	105.658
	μ neutrino	ν_μ	0	$< 0.19 \times 10^{-6}$
Third	tau	τ	-1	1776.82
	τ neutrino	ν_τ	0	$< 18.2 \times 10^{-6}$

There are four fundamental forces in nature: the strong force, the weak force, the electromagnetic force, and the gravitational force. They have different working ranges and strengths. Each of these forces is mediated by the exchange of the force carrier particles called mediators. All the forces, their strengths, mediators and corresponding theories are listed in Table 2.3 [1, 2]. The gravitational force is the attraction which is experienced due to the energy-mass of the particle. Since it is too weak for fundamental particles, it does not have a significant role in elementary particle physics. The electromagnetic force is the other long range force which acts between two electrically charged particles. The strong force acts only between quarks. At low energies, it is stronger than the electromagnetic force and it holds the quarks together to form particles that are made up of quarks. The weak force acts between both quarks and leptons. It can change particles from one type to another. For example, the electron can be changed to the electron neutrino by the weak interaction; however, it cannot be changed into a muon or muon neutrino. Like leptons, a quark can be turned into another

quark within the generations by the weak force. But with a much reduced effect, it can act across the quark generations [3, 14].

Table 2.3: The fundamental forces.

Force	Strength	Mediator	Theory
Strong	1	Gluon (g)	Chromodynamics
Electromagnetic	10^{-2}	Photon (γ)	Electrodynamics
Weak	10^{-7}	W^\pm and Z^0	Flavordynamics
Gravitational	10^{-39}	Graviton (G)	Geometrodynamics

Feynman diagrams are the representation of the interactions between particles. In these diagrams, interactions of particles are represented by points, called vertices. In Feynman diagrams, the time can be either represented on horizontal or vertical axis. In this thesis it is chosen to represent the time on horizontal axis and the space on the vertical axis. The Feynman diagrams are purely symbolic and the aim of them is to show the overall process, so the actual values of time and space are not important. Some examples of Feynman diagrams, which describe the pair annihilation, pair production and Compton scattering, are shown in Figure 2.1.

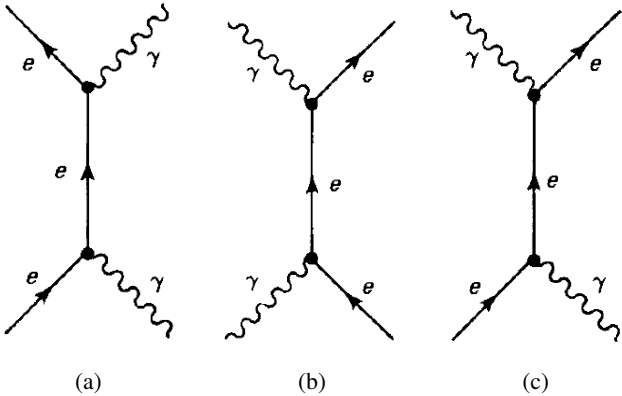


Figure 2.1: Examples of Feynman diagrams: (a) pair annihilation, (b) pair production (c) Compton scattering.

Quantitatively, each diagram stands for a particular number which is calculated by *Feynman Rules* and represents the contribution of the diagram to the physical process. In this calculation each vertex introduces a factor of α which is the coupling constant. The transition strength or the transition probability, which is the quantity observed experimentally, is proportional to the square of the coupling constant [1, 16].

2.2 Quantum Chromodynamics

Quantum chromodynamics (QCD) is the theory of interactions of gluons and quarks. It is a more complicated theory than the other theories: quantum electrodynamics (QED), the theory of interactions of photons with charged particles, and the flavordynamics, the theory of interaction of W^\pm and Z^0 with quarks and leptons.

One of the reasons of this complication comes from the coupling constants of the interactions. If the coupling constant of an interaction is small, it can be described by simple diagrams with a few vertices. The coupling constants of electromagnetic and weak interactions are small, however; in QCD the coupling constant depends on the separation between the particles. In long distances, i.e. low energies, the coupling constant is of the order of 1, which makes the contribution from the diagrams with many vertices as much important as the ones with few vertices. So, the perturbation theory is not valid in low energies. While the separation between particles gets smaller, i.e. in higher energies, the coupling constant decreases which makes it possible to use perturbative QCD [16].

Color, like electric charge in QED, is a property that causes to experience the strong force. However, where there is one kind of charge (positive or negative) in QED, there are three kinds of color in QCD: red, blue, green. A quark carries one of these colors whereas an anti-quark one anti-color. A gluon carries one color and one anti-color. A quark can change its color in a vertex as shown in Figure 2.2. Since gluons have color, they can interact to other gluons. There are two possible vertices: three-gluon vertex and four-gluon vertex, shown in Figure 2.3.

Quarks are confined in colorless packages, i.e. the particles that can be seen in nature are colorless. The confinement of all three color creates a colorless package as well as the confinement of a color with its anti-color. As a result of this confinement, it is impossible to

observe a single quark or a single gluon in the laboratory [1].

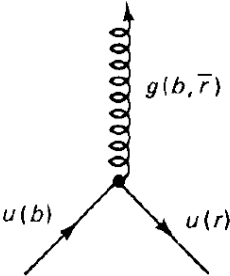


Figure 2.2: A strong interaction vertex.

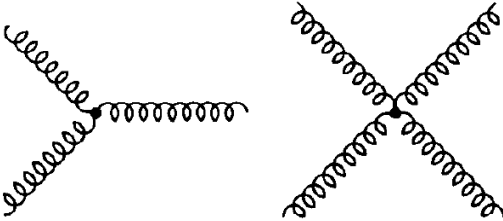


Figure 2.3: Gluon-gluon vertices. Left: three-gluon vertex, right: four-gluon vertex.

2.3 Prompt Photon Production in Experiments

The expression *prompt photons* stands for the photons not coming from the decay of hadrons but produced at large transverse momenta. In high energy proton-proton collisions, single prompt photons are produced by quark-gluon Compton scattering and quark-antiquark annihilation, see Figure 2.4.

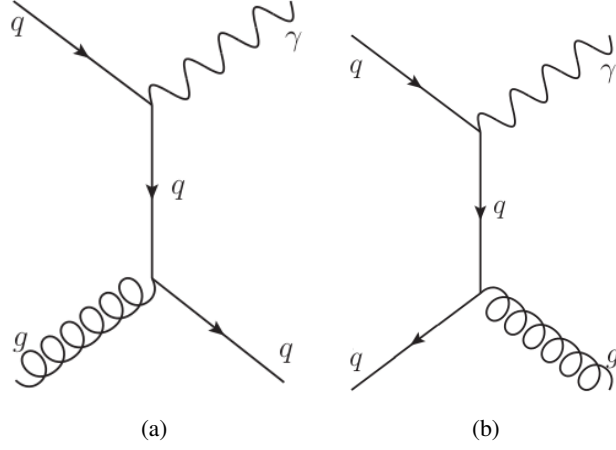
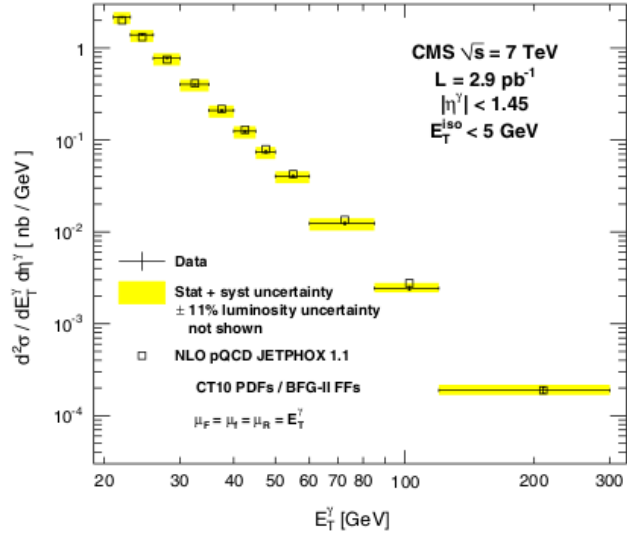


Figure 2.4: Feynman diagrams contributing to photon production: (a) quark-gluon Compton scattering, (b) quark-antiquark annihilation.

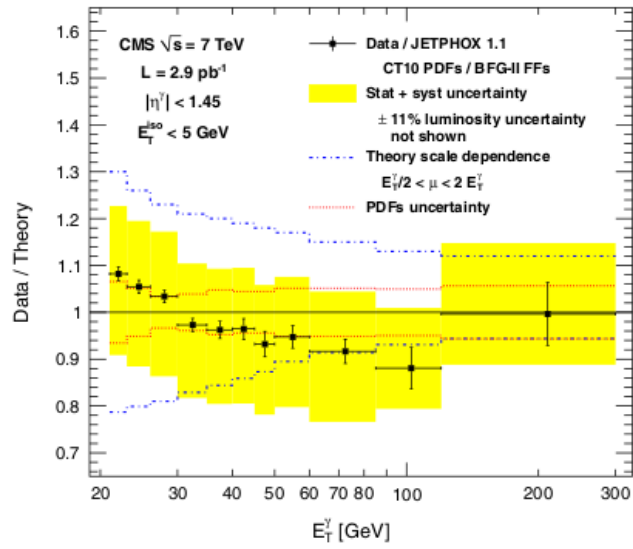
The differential cross section, the measure of the likelihood of interaction between particles, is defined as

$$\frac{d^2\sigma}{dE_T d\eta} = \frac{N^\gamma \cdot U}{L \cdot \epsilon \cdot \Delta E_T \cdot \Delta \eta} \quad (2.1)$$

where N^γ is the signal photon yield measured from data, L is the integrated luminosity, U denotes the corrections for finite detector resolution, ϵ is the product of the efficiencies, and ΔE_T and $\Delta \eta$ are the sizes of the E_T and η bins that are used in the analysis. The result of the differential cross section measurement of the prompt photon production using the CMS Experiment is presented in Figure 2.5(a) and the comparison of the results with the theory is shown in Figure 2.5(b). The result and its comparison with theory for ATLAS Experiment is shown in Figure 2.6. As it can be seen from the comparisons, the results agree with theory [5, 6].

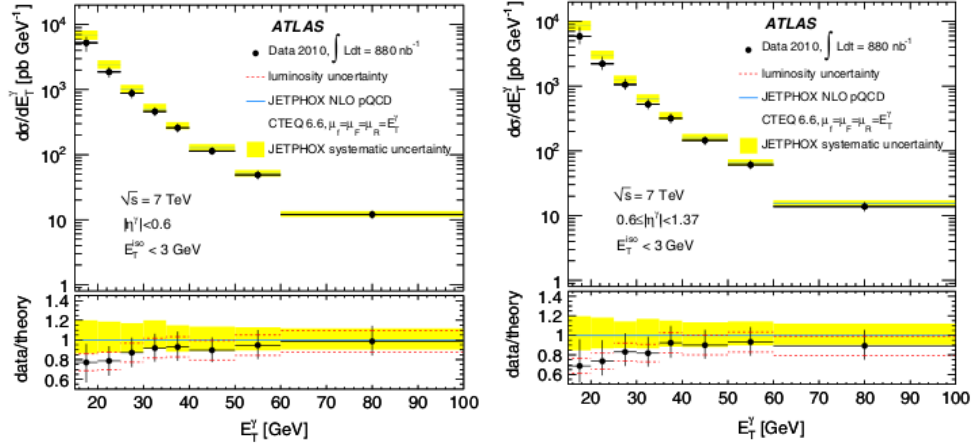


(a) Measurement of cross section



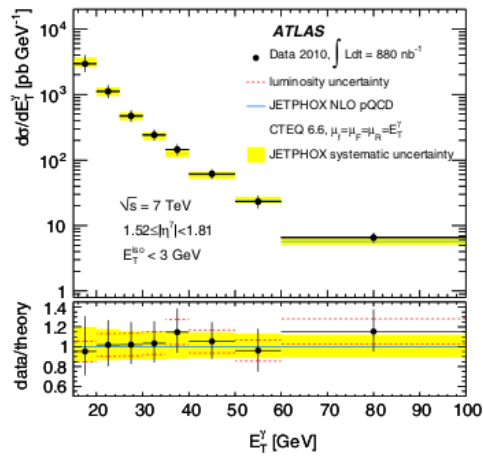
(b) Comparison with theory

Figure 2.5: Measured differential isolated prompt photon cross section using CMS Experiment.



(a) $|\eta| < 0.6$

(b) $0.6 < |\eta| < 1.37$



(c) $1.52 < |\eta| < 1.81$

Figure 2.6: Measured differential isolated prompt photon cross section using ATLAS Experiment.

CHAPTER 3

THE CMS EXPERIMENT

The Compact Muon Solenoid (CMS) experiment [8, 9] uses a multi-purpose detector operates at the Large Hadron Collider (LHC) at CERN to investigate a wide range of physics, including the search for the Higgs boson, extra dimensions, and particles that could make up dark matter.

3.1 The Large Hadron Collider (LHC)

The Large Hadron Collider (LHC) is a 27 km two-ring-superconducting-hadron accelerator and collider near Geneva, where it spans the border between Switzerland and France about 100 m underground, see Figure 3.1. There are six experiments at the LHC, two large experiments ATLAS and CMS, two medium-size experiments ALICE and LHCb and two smaller experiments TOTEM and LHCf. The two large experiments, ATLAS and CMS, are general purpose detectors to analyze largest range of physics. They are designed independently to make the cross-confirmation of any new physics discoveries possible. One of the medium-size experiment, ALICE, has specialized detector for analyzing the quark-gluon plasma which will be created by colliding heavy ions and is believed to have existed soon after the Big Bang. Whereas the other medium-size experiment, LHCb, has designed for analyzing the differences between matter and antimatter by studying b quark. The two smaller experiments, TOTEM and LHCf, are designed to study on *forward particles* (protons or heavy ions) which are the particles that just brush past each other as the beams collide, rather than meeting head-on [13].

The detector used in this study, CMS, uses data obtained by colliding two proton beams. The journey of protons (Figure 3.2) starts by removing electrons from hydrogen atoms. Protons are injected from linear accelerator (LINAC2) into Proton Synchrotron (PS) Booster. From

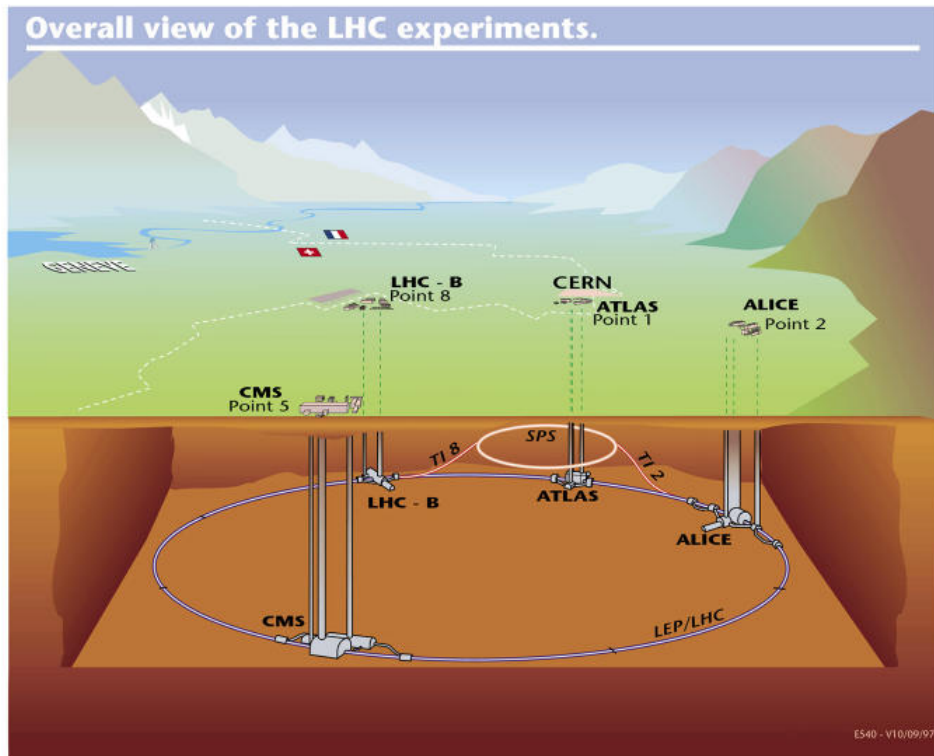


Figure 3.1: The Large Hadron Collider (LHC).

PS Booster protons are transferred to Proton Synchrotron (PS) which accelerates them up to 25 GeV. Then, by the Super Proton Synchrotron (SPS) they are accelerated up to 450 GeV. Finally, they end up with the Large Hadron Collider and reach the energy up to 7 TeV [13].

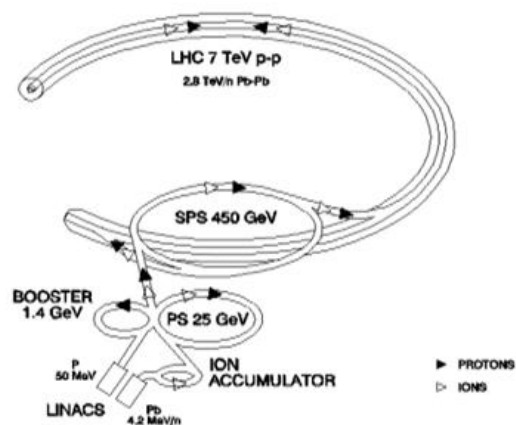


Figure 3.2: CERN Accelerator Complex.

The world's highest energy particle accelerator, LHC, accelerated its twin proton beams to an energy of 3.5 TeV in March 2010 [17]. The data taken during 2010 is analyzed in this study.

3.2 The CMS Detector

The traveling proton beams collide at the center of the CMS detector and create a wide range of particles. To detect all of these particles CMS consists of different layers of detector (Figure 3.3). Each layer of detector is designed to stop and measure the different particles (Figure CMS-layer). The innermost layer, tracking chamber (Tracker), is designed to detect all charged particles. Next layer, electromagnetic calorimeter (ECAL), measures the energy of electrons and photons while hadron calorimeter (HCAL) measures the energy of any particle made up of quarks. The outermost layer, muon chamber, measures muons. The ECAL and HCAL absorb all energy of their detecting particle and stop them while tracking and muon chamber do not [18].

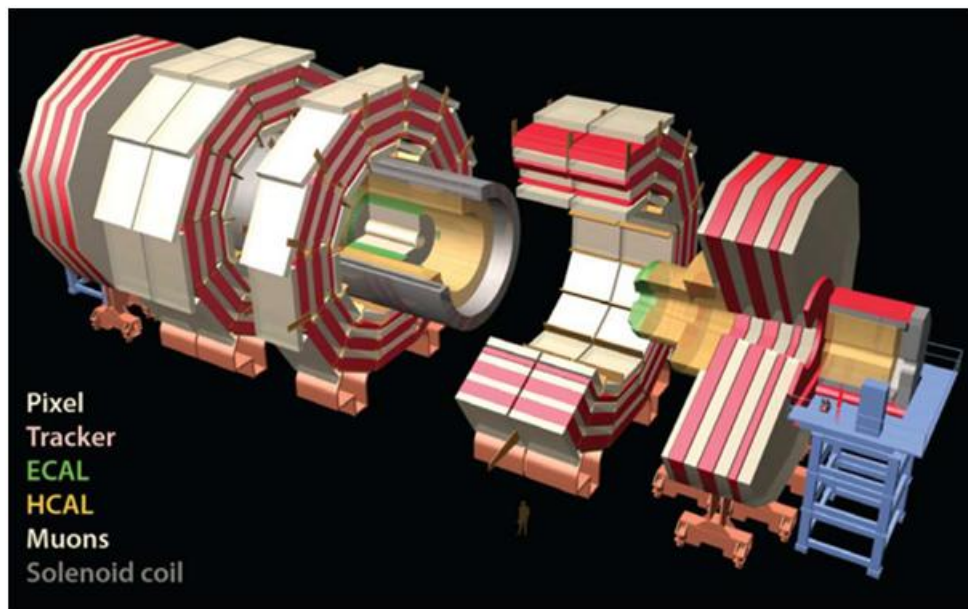


Figure 3.3: The CMS detector.

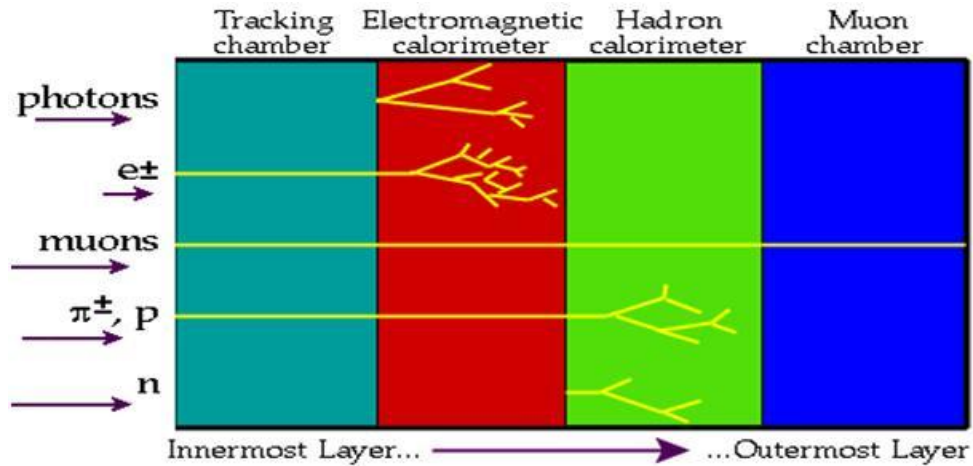


Figure 3.4: The CMS detector layers.

3.2.1 Coordinate Conventions

The CMS coordinates are adjusted to have the origin centered at the nominal collision point. The y-axis pointing vertically upward, and the x-axis pointing radially inward toward the center of the LHC. Thus, the z-axis points along the beam direction toward the Jura mountains from LHC Point 5 (see Figure 3.1). The azimuthal angle ϕ is measured from the x-axis in the x-y plane. The polar angle θ is measured from the z-axis. Pseudorapidity is defined as $\eta = -\ln \tan(\theta/2)$. Hence, the transverse momentum (p_T) and energy (E_T) to the beam direction, are computed from the x and y components. The imbalance of energy measured in the transverse plane is denoted by E_T^{miss} [9].

3.2.2 Inner Tracking System

The inner tracking system is designed to provide a precise measurement of the trajectories of charged particles and reconstruction of secondary vertices. It surrounds the interaction point with its 5.8 m length and 2.5 m diameter. It is composed of pixel detector and silicon strip tracker. The acceptance of the tracker system is extended up to a pseudo-rapidity of $|\eta| < 2.5$. The CMS tracker system is the largest silicon tracker ever built with a 200 m² of active silicon area [8].

3.2.2.1 Pixel Detector

The closest part of the tracking system to the interaction region is the pixel system. It is important for good secondary vertex reconstruction since contributes to the precise tracking points in $r - \phi$ and z . The pixel detector is responsible for forming seed tracks for the outer track reconstruction and high level triggering. It has three barrel layers (BPix) at radii between 4.4 cm and 10.2 cm. It is completed by 2 disks (FPix) in the endcaps. The BPix layers, which have length of 53 cm, are located at mean radii of 4.4, 7.3 and 10.2 cm (see Figure 3.5). They have 48 million pixels covering a total area of 0.78 m^2 . The FPix disks extending from 6 to 15 cm in radius and placed on each side at $z = \pm 34.5$ and $z = \pm 46.5$ cm (see Figure 3.5). They cover the 0.28 m^2 area with 18 million pixels. The arrangement of the 3 barrel layers and the forward pixel disks on each side gives 3 tracking points over almost the full η -range [8].

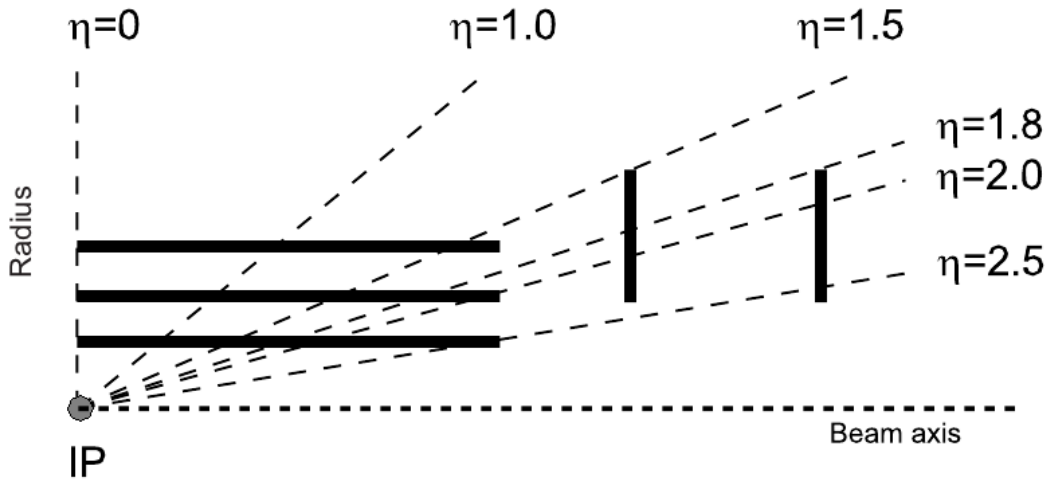


Figure 3.5: Geometrical layout of the pixel detector.

3.2.2.2 Silicon Strip Tracker

The silicon strip tracker has 10 barrel detection layers extending outwards to a radius of 1.1 m. It is completed by 3 plus 9 disks in the endcaps. The tracker silicon strip detector consists of four inner barrel (TIB) layers and an outer barrel (TOB) consists of six concentric layers. The TIBs are assembled in shells with two inner endcaps (TID), which are all composed of

three small discs (see Figure 3.6). Finally, there are two endcaps (TEC) which close off the tracker. Each layer has silicon modules designed differently for its place within the detector. The silicon strip tracker is composed of 15148 detector modules distributed among the four different subsystems (TIB, TID, TOB, TEC). Each module carries either one thin ($320\ \mu\text{m}$) or two thick ($500\ \mu\text{m}$) silicon sensors from a total of 24 244 sensors. Silicon sensors are highly suited to receive many particles in a small space due to their fast response and good spatial resolution [8, 18].

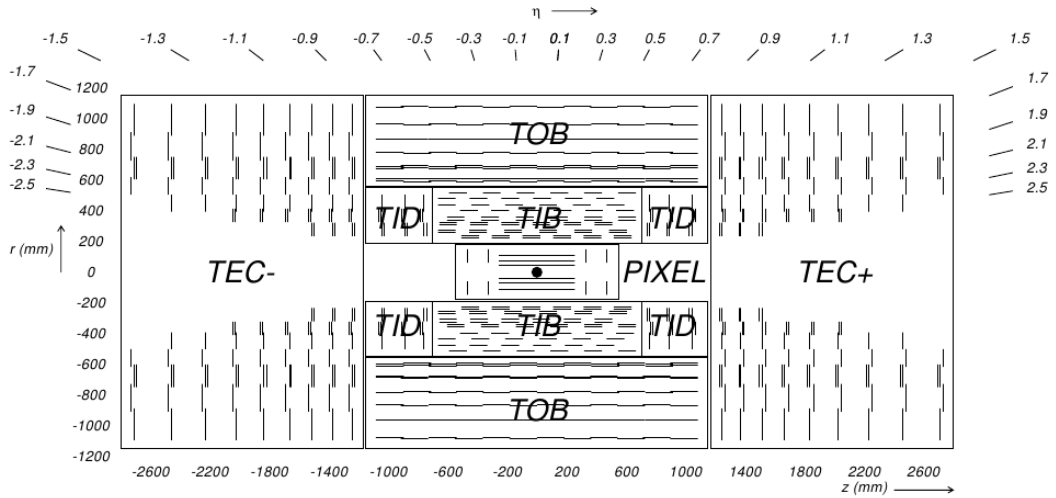


Figure 3.6: Schematic cross section through the CMS tracker system.

3.2.3 Electromagnetic Calorimeter

The CMS electromagnetic crystal calorimeter (ECAL) was designed to have both excellent energy resolution and high granularity, making it a powerful instrument to measure photons with high precision at LHC. It is divided into three regions: the barrel region (EB) which covers the pseudorapidity range $|\eta| < 1.479$, the endcap region (EE) covering the pseudorapidity range $1.479 < |\eta| < 3.0$ and the region of preshower detector, which is placed in front of the EE, covering the pseudorapidity range $1.653 < |\eta| < 2.6$ (see Figure 3.7). ECAL is mainly made of lead tungstate ($PbWO_4$) crystals. There are 61200 crystals placed in EB and 7324 crystals in each of the EE. In the barrel region Avalanche photodiodes (APDs) are used as photodetectors whereas vacuum photodiodes (VPTs) are used in the endcaps. Because of

its fast and radiation-hard characteristics, lead tungstate crystals are chosen to be used. Due to the use of high density crystals, the design of ECAL is fast, has fine granularity and is radiation resistant, which are all important features in the LHC environment [8, 9].

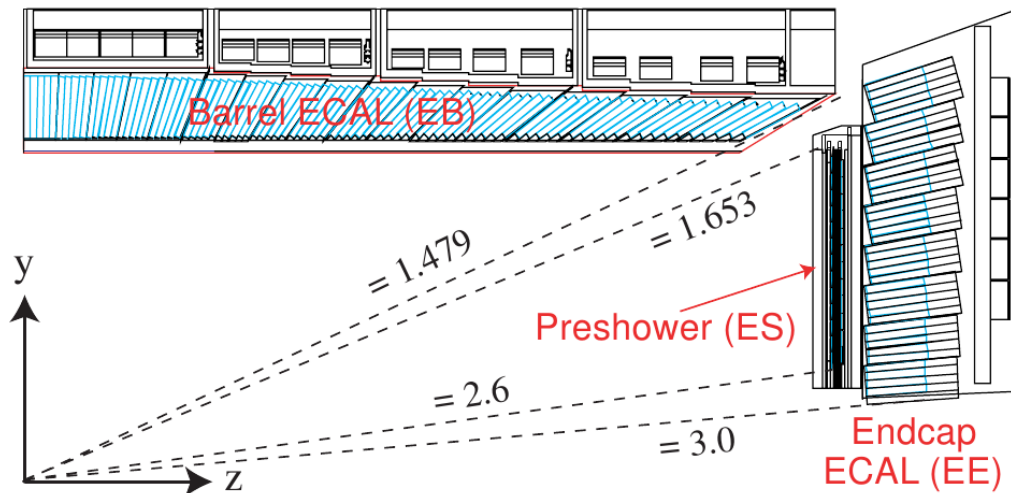


Figure 3.7: Transverse view of the electromagnetic calorimeter (ECAL).

3.2.3.1 Lead Tungstate Crystals

When electrons and photons pass through those crystals, lead tungstate crystal scintillates i.e. produces light in proportion to the energy of the incident particle. The advantage of these crystals are that they produce light in fast, short, well-defined photon bursts that allow for a precise, fast and fairly compact detector. The scintillation decay time is in the same order of magnitude with the LHC bunch crossing time. The 80% of the light is emitted in 25 ns. The output of the light is about 4.5 photoelectrons per MeV, which is relatively low. Hadrons does cause a cumulative reduction of light transmission. However; the damage will remain within limits required for good ECAL performance [8, 9].

3.2.3.2 Photodetectors

The light output coming from the lead tungstate crystal is collected by the avalanche photodiodes (APDs) in EB and by the vacuum phototriodes (VPTs) in EE. Each APD has an active

area of $5 \times 5 \text{ mm}^2$ and at the back of each crystals there are 2 APDs glued. Each VPT has 25 mm in diameter with an active area $\approx 280 \text{ mm}^2$ and a VPT is glued to the back of each crystals (see Figure 3.8).

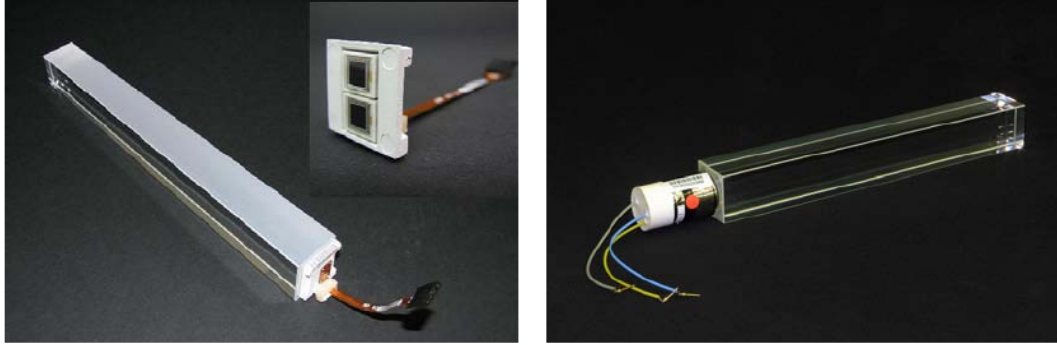


Figure 3.8: Lead tungstate crystals with photodetectors attached. Left: A crystal in barrel inserted a capsule with two APDs. Right: A crystal in endcap with a VPT attached.

Avalanche photodiodes (APDs) are made of semiconducting silicon with a strong electric field applied to them. When a scintillation photon hits the silicon it takes an electron out of an atom. Because of the applied electric field, the electron is accelerated. Then, it hits other atoms and takes electrons off those too. And those electrons will be accelerated too. As the procedure continues, the number of avalanche electrons will increase exponentially. Hence, APDs are able to produce a very high current in a short time. This characteristic is necessary, since the lead tungstate crystals give low yield of light for incident particles. Finally, the signal is amplified, digitized and immediately transported away by fibre optic cables, so that the analysis can be done away from the radiation area.

Vacuum phototriodes (VPTs) are used in the endcaps because of high radiation, which is not suitable for the use of silicon photodiodes. A VPT contains three electrodes placed in a vacuum. Like in APDs, when light hits atoms, electrons are released. Because of the voltage difference between electrodes, electrons are accelerated into the second electrode (the anode). There electrons hits the anode and produce several more electrons, which are all accelerated to the third (the dynode), releasing even more electrons. Hence, VPDs also creates a large current from the low yield of scintillation light. Finally, like in APDs, the signal is turned into digital signal and transported away by the optic fibres to the upper level readout [9, 18].

3.2.3.3 Preshower Detector

The main purpose of the preshower detector (ES) is to identify neutral pions in the endcaps within a region $1.653 < |\eta| < 2.6$. Since it has high granularity, it also helps the identification of electrons against minimum ionizing particles, and improves the position determination of electrons and photons. ES is a sampling calorimeter consists of two layers and has total thickness of 20 cm. The first layer, lead radiators, initiate electromagnetic showers from incoming photons or electrons. The second layer, silicon strip sensors, placed after each radiator. They measure the energy deposited and the transverse shower profiles.

3.2.4 Hadronic Calorimeter

The Hadron Calorimeter (HCAL) is particularly important for the measurement of the hadron jets and particles such as neutrinos or exotic particles that are resulting in the apparent missing transverse energy. This determination of missing energy is a crucial signature for new particles and phenomena, such as it will be encountered in the searches for the supersymmetric partners of quarks and gluons.

HCAL is a sampling calorimeter, meaning it finds the position, energy and arrival time of the particle using alternating layers of absorber and fluorescent scintillator materials. Since the magnetic field is 4T, calorimeter absorber should be non-magnetic to eliminate magnetic forces on it, and to avoid distortion. It should be a structural material, because it must support itself as well as all other interior components. Also, it must be affordable. Due to these requirements, a copper alloy (70% Cu, 30% Zn) is chosen. Scintillation is re-emitting the absorbed energy from an incoming particle in the form of a small flash of light. The scintillation light is converted by wavelength-shifting (WLS) fibres embedded in the scintillator tiles and channeled to photodetectors via clear fibres. This light is detected hybrid photodiodes, (HPDs) that can provide gain and operate in high axial magnetic field.

HCAL consists of four subdetectors (see Figure 3.9): barrel calorimeter (HB), endcap calorimeter (HE), outer calorimeter (HO) and forward calorimeter (HF). HB covers the pseudorapidity range $|\eta| < 1.3$ whereas HE covers the range $1.3 < |\eta| < 3.0$, a region containing about 34% of the particles produced in the final state. Because of the high luminosity of the LHC, HE designed to handle high counting rates and have high radiation tolerance. The hadron

calorimeter is extended outside the solenoid in the $|\eta| < 1.3$ region with HO since the combined stopping power of EB plus HB does not provide sufficient containment for hadron showers. Finally, there are two forward calorimeters (HF+ and HF-) positioned at either end of CMS. It detects the particles coming out of the collision region at shallow angles relative to the beam line. HF will experience very high particle fluxes. So HF is designed to survive in these harsh conditions for at least a decade [8, 9].

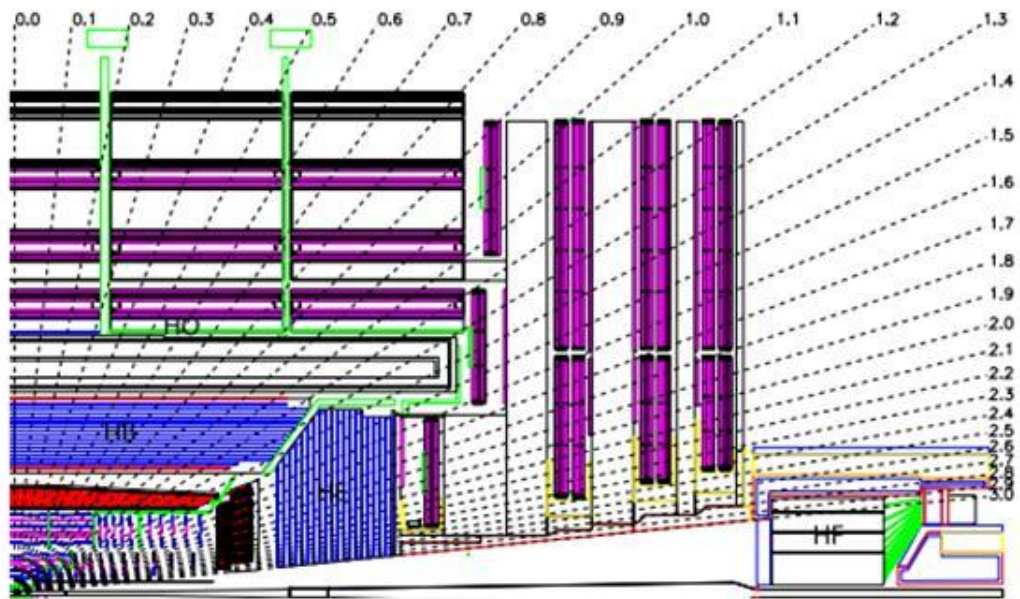


Figure 3.9: Longitudinal view of the CMS detector showing the locations of the hadron barrel (HB), endcap (HE), outer (HO) and forward (HF) calorimeters.

3.2.5 Muon System

Muon detection is a powerful tool for recognizing signatures of most of the physics that LHC is designed to explore over the very high background rate expected at LHC with full luminosity. For example, the predicted decay of the Standard Model Higgs boson into ZZ or ZZ^* , which in turn decay into 4 leptons, has been called *gold plated* for the case in which all the leptons are muons. Therefore, as is implied by the middle name of the experiment, the precise detection of muons is of central importance to CMS. The muon system has 3 functions: muon identification, momentum measurement, and triggering. Good muon momentum resolution

and trigger capability are enabled by the high-field solenoidal magnet and its flux-return yoke. The latter also serves as a hadron absorber for the identification of muons.

The muon system uses three different technologies to detect and measure the muons: drift tubes (DT) in the barrel region, cathode strip chambers (CSC) in the endcap region and resistive plate chamber (RPC) in both the barrel and endcap region (Figure 3.10). The barrel drift tube (DT) chambers cover the pseudorapidity region $|\eta| < 1.2$ and the number of chambers and their orientation are chosen to provide good efficiency for detecting muon hits and for rejecting background hits. The CSCs have fast response time, fine segmentation, and are radiation resistance. Due to these characteristics they are chosen to be used in the region $0.9 < |\eta| < 2.4$ where the muon rates and background levels are high and the magnetic field is large and non-uniform. Because of the uncertainty in the eventual background rates and in the ability of the muon system to measure the correct beam-crossing time when the LHC reaches full luminosity, a complementary, dedicated trigger system consisting of resistive plate chambers (RPC) was added in both the barrel and endcap regions. The RPCs provide a fast, independent, and highly-segmented trigger with a sharp p_T threshold over a large portion of the rapidity range ($|\eta| < 1.6$) of the muon system. The RPCs are double-gap chambers, operated in avalanche mode to ensure good operation at high rates. They produce a fast response, with good time resolution but coarser position resolution than the DTs or CSCs [8, 9].

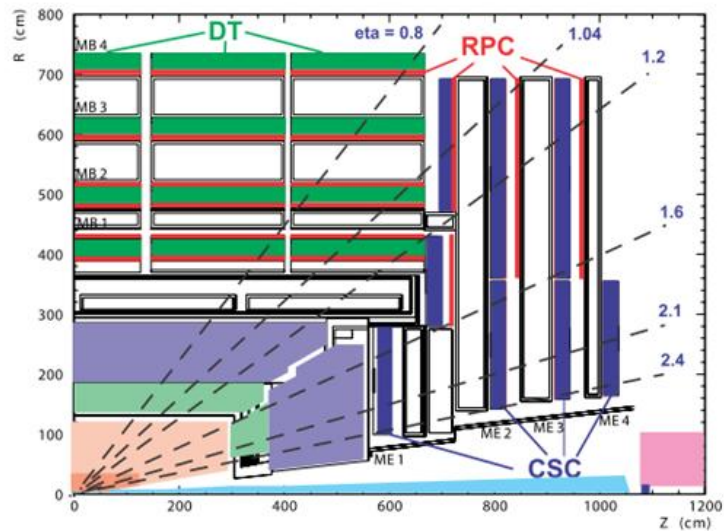


Figure 3.10: Longitudinal view of the muon system.

3.2.6 Superconducting Magnet

An important aspect driving the detector design and layout is the choice of the magnetic field configuration for the measurement of the momentum of muons. Large bending power is needed to measure precisely the momentum of high-energy charged particles. This forces a choice of superconducting technology for the magnets. A solenoid (see Figure 3.11) was preferred to provide a field parallel to the beams, so that the bending of the muon track is in the transverse plane. A strong magnetic field enables an efficient trigger, high mass resolution and maximum benefit from a crystal electromagnetic calorimeter [8, 9].

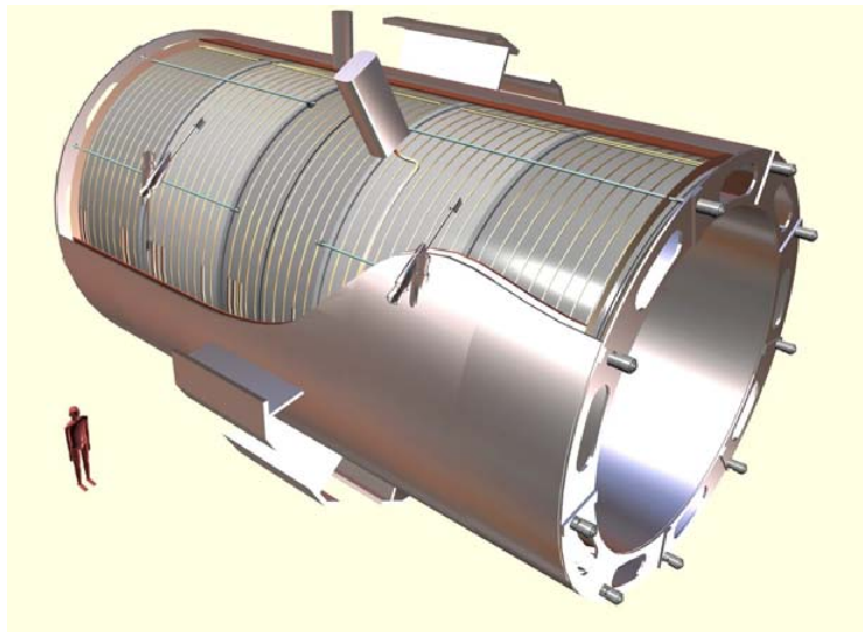


Figure 3.11: Superconducting magnet of CMS.

3.3 Trigger System and Data Acquisition

LHC is aimed to provide proton-proton collisions at high interaction rates, the interactions take place at every 25 ns and several collisions occur at each crossing of proton bunches depending on luminosity. At its peak performance, one billion interaction will occur in every second inside the CMS and it is impossible to store all the data. Therefore, trigger system is used to select potentially interesting events and reduce the rate to a few events per second.

This process is done in two steps. First is Level-1 (L1) trigger which is a custom-designed and largely programmable electronics. This trigger involves the calorimeter, muon systems and some correlation of information between them. The L1 selection depends on some E_T or p_T threshold sets of the *trigger primitive* objects such as photons, electrons, muons and jets. It also put some selection to the global sum of E_T and E_T^{miss} . Second step is High-Level Trigger (HLT) which is a software system implemented in a filter farm of about one thousand commercial processors. In the HLT software various strategies are applied. In this process, by the help of the software, only objects that are actually needed are reconstructed. In this way, partial reconstruction can be done and many virtual trigger levels can be used. For example, calorimeter and muon information, followed by use of the tracker pixel data and finally the use of the full event information (including full tracking) can be used to select events [8, 9, 18].

The L1 trigger is designed to reduce the rate of accepted events to a maximum of 100 kHz. During the L1 selection period, all the high-resolution data is held in pipelined memories. After L1 acceptance, the data is transferred from the pipelines to front-end readout buffers. There with the help of the DAQ system, further signal processing, zero-suppression and/or data-compression, are held and then the data are placed in dual-port memories for access. The HLT reduce the L1 output rate of 100 kHz to 100 Hz for storage. The functionality of DAQ/HLT system is to perform the readout of the front-end electronics, to execute the physics selection to accept the interesting events and forward these events to the online services to monitor detector performance. The DAQ system also operates the Detector Control System (DCS) which is important to obtain high-quality physics data with the safe operation of CMS [8, 9, 10].

CHAPTER 4

ISOLATED PHOTON ANALYSIS

4.1 Motivation

There are several motivations of photon production study at hadron colliders. First of all, it provides a test of perturbative quantum chromodynamics (pQCD) over several order of magnitudes. Moreover, it represents an irreducible background for many new physics searches, such as $H \rightarrow \gamma\gamma$, SUSY and extra-dimensions. Furthermore, it provides an ideal playground for the commissioning of the identification techniques used to study final states with isolated photons.

In high-energy pp collisions, prompt photons can be produced through either the quark-gluon Compton scattering $qg \rightarrow q\gamma$ or quark pair annihilation $q\bar{q} \rightarrow g\gamma$. Another contribution to the inclusive photon production comes from the fragmentation of colored partons from other QCD processes [19].

4.2 Data and simulation samples

The data sample, recorded in 2010 with the CMS detector, used in this analysis corresponds to a total integrated luminosity of $35.9 \pm 1.4 pb^{-1}$ [20]. Run ranges and the path of these data sets is given in Table 4.1. The applied High Level Trigger (HLT) paths are summarized in Table 4.4 [21].

Table 4.1: Summary of analyzed data.

Run Range	Data sets
136035-144114	/EG/Run2010A-Dec22ReReco_v1/AOD
146428-149294	/Photon/Run2010B-Dec22ReReco_v1/AOD

The simulation samples were generated using the CTEQ6L parton distribution functions and the Z2 parameter set with PYTHIA version 6.4.20 [22]. Generated events are reconstructed using the same algorithm as for the data after they are passed through the full GEANT 4 simulation of the CMS detector. For the simulation two sets of samples generated using PYTHIA: one is for the signal (summarized in Table 4.2), which contains isolated direct and fragmentation photons, and the other is for background (summarized in Table 4.3), which contains all other photons. In the simulation, a signal photon must have an isolation sum of less than 5 GeV to imitate the isolation requirement at the reconstruction level. The isolation sum is calculated as the sum of the E_T of all charged and neutral particles within a cone of radius $R = 0.4$ where $R \equiv \sqrt{(\eta^{other} - \eta^\gamma)^2 + (\phi^{other} - \phi^\gamma)^2}$. The 5 GeV threshold at the generator level reduce the contribution from fragmentation photons, guarantee the direct photon efficiency to be greater than 95% and minimize dependence of the efficiency on the variation of underlying event models [20].

Table 4.2: Summary of MC samples for signal used in the analysis. Full names of all sets have extension `_TuneZ2_7TeV_pythia6/Fall10-START38_V12-v1/GEN-SIM-RECO`.

\hat{p}_T range, GeV/c	MC set	# events	σ , pb
0-15	/G_Pt_0to15	9.6×10^5	8.4×10^7
15-30	/G_Pt_15to30	8.3×10^5	1.7×10^5
30-50	/G_Pt_30to50	9.3×10^5	1.7×10^4
50-80	/G_Pt_50to80	1.0×10^6	2.7×10^3
80-120	/G_Pt_80to120	1.0×10^6	4.5×10^2
120-170	/G_Pt_120to170	1.0×10^6	8.4×10^1
170-300	/G_Pt_170to300	1.1×10^6	2.3×10^1
300-470	/G_Pt_300to470	1.1×10^6	1.5×10^0
470-800	/G_Pt_470to800	1.1×10^6	1.3×10^1

Table 4.3: Summary of MC samples for background used in the analysis. Full names of all sets have extension `_TuneZ2_7TeV_pythia6/Fall10-START38_V12-v1/GEN-SIM-RECO`.

\hat{p}_T range, GeV/c	MC set	# events	σ , pb
0-5	/QCD_Pt_0to5	5.5×10^5	4.8×10^{10}
5-15	/QCD_Pt_5to15	1.6×10^6	3.7×10^{10}
15-30	/QCD_Pt_15to30	4.2×10^6	8.2×10^8
30-50	/QCD_Pt_30to50	2.8×10^6	5.3×10^7
50-80	/QCD_Pt_50to80	2.3×10^6	6.4×10^6
80-120	/QCD_Pt_80to120	2.4×10^6	7.8×10^5
120-170	/QCD_Pt_120to170	3.0×10^6	1.2×10^5
170-300	/QCD_Pt_170to300	3.2×10^6	2.4×10^4
300-470	/QCD_Pt_300to470	2.1×10^6	1.2×10^3
470-600	/QCD_Pt_470to600	2.0×10^6	7.0×10^1
600-800	/QCD_Pt_600to800	2.0×10^6	1.6×10^1

4.3 Event Selection

Event selection is required in order to select the interesting events and distinguish signal photons from the background. This selection is done by many steps. First of all trigger selection is applied to store the interesting events. Then vertex selection is applied to distinguish signal photons from the fake ones. Some thresholds are needed to be satisfied in the photon reconstruction process in order to avoid noises coming from the detector and measure the energy and position of photons correctly. Finally, identification and isolation selections are applied to obtain photon candidates with high purity.

4.3.1 Trigger Selection

Photon candidate events are selected on-line by two-level trigger system to have an energy deposition above a given threshold in ECAL. In the Level-1 trigger system, 5×5 crystal matrices are considered as trigger towers and the E_T sum of two neighboring trigger towers is required to be above 8 GeV. The events that satisfy this selection are passed on to the second trigger level, the High Level Trigger (HLT). In HLT, the crystals are clustered with the same clustering algorithm used in the off-line photon reconstruction [23]. The events that have at least one cluster with a E_T above a programmable threshold (E_T^{HLT}) are stored for further analysis. In this analysis, E_T^{HLT} of 20, 30, 50 and 70 GeV are used [20]. Rate-reduction

factors are applied to the triggers at 20, 30 and 50 GeV since the available trigger bandwidth was limited and the instantaneous luminosity of LHC was high. A rate-reduction factor means that a specific rate of accepted events are stored for data analysis. Therefore, a subset of the full data-set for events with photons that have $E_T < 80\text{GeV}$ is used. The effective integrated luminosities for each applied HLT paths are shown in Table 4.4.

Table 4.4: Summary of HLT paths.

Run range	HLT Path	$\int Ldt \text{ pb}^{-1}$
138564-143962	HLT_Photon20_Cleaned_L1R	2.46
144010-147116	HLT_Photon30_Cleaned_L1R	5.81
147196-148058	HLT_Photon50_Cleaned_L1R_v1	9.47
148822-149294	HLT_Photon70_Cleaned_L1R_v1	18.4

4.3.2 Vertex Selection

In order to reduce the events not coming from pp collisions, a good primary interaction vertex is required to be reconstructed. Such vertices must have at least three tracks. Also these vertices must be within 24 cm along the beam axis and 2 cm perpendicular to the beam axis with respect to the nominal center of the detector. Moreover, in each event at least 25% of the reconstructed tracks are required to be of good quality [20].

4.3.3 Photon Reconstruction

The presence of material in front of ECAL can cause conversion of photons into electron-positron pairs and bremsstrahlung from electrons and positrons. Then, due to the strong magnetic field, the energy flow which comes from primary electrons or converted primary photons spread over in ϕ direction with increasing distances from the collision vertex within the tracker. The trajectory in the r-z plane is not affected by the magnetic field. In order to collect these spread photon energy in ECAL, clusters are summed into superclusters (SCs)

which are extended in ϕ . The clustering threshold in transverse energy is taken approximately 1 GeV and the algorithms used are: hybrid (in EB) and Multi 5×5 (in EE) algorithms.

4.3.3.1 Hybrid Algorithm

Hybrid algorithm uses the η - ϕ geometry of the barrel crystals. While searching dynamically for separated energy in the ϕ direction, by taking a fixed bar of 3 or 5 crystals in η , it makes good use of the knowledge of the lateral shower shape in the η direction. The procedure is as follows:

- First, a seed crystal needed to be found. For this, at each step the crystals, not already belonging to a cluster, are scanned in decreasing energy order. A minimum threshold ($E_T^{hybseed}$) is required in order to avoid low energy backgrounds and noise contamination. The crystal that has the higher E_T , which satisfies the $E_T > E_T^{hybseed}$, is selected as seed.
- Next, a 3×1 domino of crystals is constructed in η - ϕ direction. These domino crystals are located to have the seed crystal at its center in η . If the central crystal of the domino has the energy greater than E_{wing} , then a 5×1 domino is used. In this way clustering proceeds N_{steps} crystals in each ϕ direction from the seed. Dominoes with energy less than E_{thresh} are eliminated.
- The dominoes are further clustered in ϕ . Each distinct cluster of dominoes is required to have a seed domino with energy greater than E_{seed} .
- The algorithm continues until all the crystals have been scanned.

The hybrid clustering algorithm is illustrated in Figure 4.1 and the parameters used are indicated in Table 4.5. As a result the hybrid super-clusters are formed up to 35 wide in ϕ and 5 wide in η direction [20, 23, 24, 25, 26].

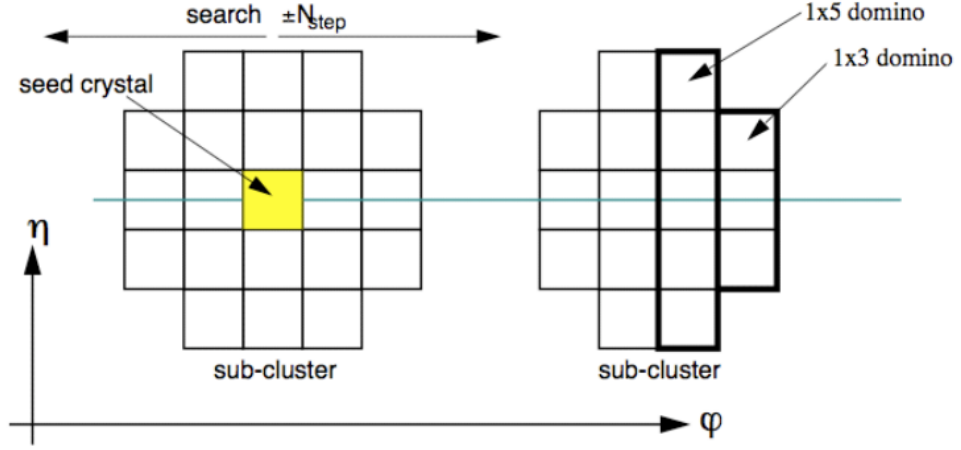


Figure 4.1: Illustration of Hybrid clustering algorithm.

Table 4.5: Usual values of the Hybrid clustering algorithm parameters.

Parameter	Default
N_{steps}	17 crystals
$E_T^{hybseed}$	1 GeV
E_{wing}	0 GeV
E_{thresh}	0.1 GeV
E_{seed}	0.35 GeV

4.3.3.2 Multi 5×5 Algorithm

The hybrid algorithm can not be used in the endcap region since the crystals are not arranged in η - ϕ geometry. However; a similar algorithm should be applied to collect energy deposits in η and ϕ . The Multi 5×5 algorithm, which is slightly different from hybrid algorithm, proceeds as follows:

- The crystals, not already belonging to a cluster, are scanned in decreasing energy order. The crystal that has the higher E_T , which satisfies the minimum threshold $E_T > E_T^{seed}$, is selected as seed.

- Then, the crystal energy is compared to its four neighbors by side in a Swiss Cross pattern in order to check to being a local maximum. If the crystal is not a local maximum, the algorithm returns back to the first step.
- Around the seed crystal, a basic cluster is constructed using the 5×5 matrix of crystals, the ones that does not belong to any cluster are included only.
- Next step is to form super-clusters by clustering basic-clusters. In order to do this, all the basic-clusters are scanned in descending order of E_T . The outer crystals around the basic cluster are searched for a secondary seed, which is required to satisfy the condition: $E_T > E_T^{bc}$. A rectangular window along η and ϕ , which is extended in the ϕ direction, is created around the secondary seed and the energy deposits inside this window are added to form super-clusters.
- The algorithm continues until all the crystals have been scanned.

During the whole procedure, the constraint that each crystal (basic-cluster) can be belong to only one basic-cluster (super-cluster) is applied. The Multi 5×5 algorithm is illustrated in Figure 4.2 and the parameters used are indicated in Table 4.6. In order to recover the energy deposited in the preshower, the EE cluster positions are extrapolated to the ES where the preshower clusters are built. The total endcap cluster energy is the sum of the cluster energies in EE and ES [20, 23, 25, 26].

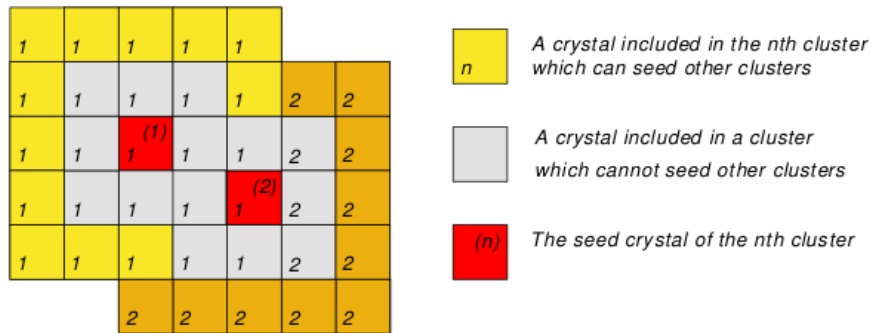


Figure 4.2: Illustration of Multi 5×5 clustering algorithm.

Table 4.6: Usual values of the Multi5 × 5 clustering algorithm parameters.

Parameter	Default
E_T^{seed}	0.18 GeV
E_{bc}	1.0 GeV

4.3.3.3 Super-cluster Position Estimation

In both algorithm, the position of super-cluster (SC) is determined by calculating the weighted mean of the position of the crystals. The weighted mean is calculated as follows:

$$x = \frac{\sum x_i \cdot W_i}{\sum W_i} \quad (4.1)$$

where x_i is the position and W_i is the log weight of crystal i . The log weight is calculated with formula below:

$$W_i = \max\left(0, W_0 + \log \frac{E_i}{E_{SC}}\right) \quad (4.2)$$

where the weight constrained to be $0 \leq W_i$. Here, W_0 , which is set to 4.7, determines the smallest fractional energy that a crystal needs to contribute to the position measurement.

Since super-clusters represents the photon candidates, the direction of photon momentum needs to be estimated from the position of super-clusters. This is done by connecting the position of the super-cluster to its the primary vertex in the event. In case there are more than one primary vertexes found, the one that has the highest scalar sum of track transverse momenta is chosen [24, 26].

4.3.3.4 Energy Corrections

The resolution of ECAL is important to any analysis which uses the electrons and/or photons. Considering the interactions with the material in front of ECAL and shower containment, energy corrections are applied to the clusters. The reconstructed photon energy is estimated by:

$$E_\gamma = F_\gamma \cdot G \cdot \sum_{i=1\dots N} c_i \cdot A_i \quad (4.3)$$

where F_γ is the correction factor applied to the super-cluster energy, G is the global scale energy calibration term, c_i is the response coefficient of i^{th} crystal to a reference, and A_i is the digital signal amplitude measured by ECAL. There are three corrections applied to this energy:

- A correction applied to EB to compensate the lateral energy leakage arising from 3° off-pointing for the η dependence. This correction is parametrized by a function $C_{EB}(\eta)$. The overall C_{EB} correction is $\lesssim 1\%$.
- Another correction arises from the different algorithm responses to the spread energy caused by the interactions with material in front of ECAL. The correction function, $f(brem)$, depends on the $brem$ parameter which describes the spread of the electromagnetic shower and defined as:

$$brem = \frac{\sqrt{\sum(\eta_i - \bar{\eta})^2 c_i A_i}}{\sqrt{\sum(\phi_i - \bar{\phi})^2 c_i A_i}} \quad (4.4)$$

where $(\bar{\eta}, \bar{\phi})$ represents the position of the super-cluster and the sum runs over all crystals in the super-cluster. This correction worths $\lesssim 7\%$ in the barrel region and $\lesssim 20\%$ in the endcap region.

- Final correction is applied due to the nonuniform distribution of the tracker material along η and the E_T dependence of the bremsstrahlung and conversion processes. This correction, $f(E_T, \eta)$, is a function of the cluster E_T and η .

Many of the effects parametrized by F_γ are only relevant in the case of converted photons and do not applied to the unconverted photons. The selection of the unconverted photons depends the the ratio of the energy deposited in the 3×3 crystal matrix to total deposited energy in the super-cluster. This ratio is called R_9 . If R_9 is greater than a specified threshold, the photon energy is reconstructed from the energy of the 5×5 matrix containing the seed crystal. In this case only the C_{EB} correction is applied [20, 23, 24, 26].

4.4 Photon Identification and Isolation

After the selections, described in previous section, are applied to the data, photon candidates are obtained. In order to increase the purity, some identification and isolation requirements are applied. First of all, photons that has the transverse momenta $p_T > 25$ GeV and no pixel seed are accepted. Second, the study is divided into four pseudo-rapidity region: central barrel ($0 < |\eta_{SC}| < 0.9$), outer barrel ($0.9 < |\eta_{SC}| < 1.4442$), low- η endcap ($1.566 < |\eta_{SC}| < 2.1$), high- η endcap ($2.1 < |\eta_{SC}| < 2.5$). This division, which excludes the transition region between barrel and endcaps ($1.4442 < |\eta_{SC}| < 1.566$), is motivated by the existence of different amount of material in front of ECAL depending on the pseudo-rapidity.

Crystals located in EB are read out with the avalanche photodiodes (APDs). Because of the direct ionizations in APD, which is called spikes, photons backgrounds are arose. Those background events are rejected by requiring the conditions described below:

- the timing measurement of the seed crystal (most energetic crystal) should be consistent with the timing of the collision.
- minimum fraction of energy to be deposited in the crystals surrounding the seed crystal and shower shape to be inconsistent with extremely narrow shower (Swiss cross, $\sigma_{in\eta}$, and $\sigma_{i\phi i\phi}$)

After these spike cleaning selections the contamination of spikes has been estimated to be less than 0.2% [21].

Furthermore, some isolation requirements are applied. The isolation variables used in this analysis described below:

- H/E : the ratio of the energy deposited in HCAL to the energy deposited in ECAL. The energies inside a cone of radius $R = \sqrt{(\Delta\eta)^2 + (\Delta\phi)^2} = 0.15$ around the reconstructed photon direction are taken into account for this measurement. This ratio is a measure of compatibility of the shower with a purely electromagnetic interaction.
- ISO_{TRK} : the scalar sum of the transverse momenta, p_T , of all tracks that are consistent with the primary vertex of the interaction. For this measurement, tracks in a hollow

cone (inner radius $R_i = 0.04$, outer radius $R_o = 0.4$) with an exclusion of η -slice ($\Delta\eta = 0.015$) are taken into account in order to avoid counting the momentum of the photon conversion tracks.

- ISO_{ECAL} : the sum of the transverse energy, E_T , deposited in ECAL inside a cone of radius $R_o = 0.4$ which is centered around the ECAL cluster. The energies inside a cone of radius $R_i = 3.5$ crystals and η -slice ($\Delta\eta = 2.5$ crystals) are not accepted to avoid mis-identification of converted photons.
- ISO_{HCAL} : the sum of the transverse energy, E_T , deposited in HCAL towers inside a hollow cone (inner radius $R_i = 0.15$, outer radius $R_o = 0.4$) which is centered around the ECAL cluster.

Compared to the background photons, signal photons should have smaller values of H/E , ISO_{TRK} , ISO_{ECAL} , and ISO_{HCAL} . Table 4.7 summarizes the set of the isolation selections applied [20, 26].

Table 4.7: Isolation cuts.

Cut	Value
H/E	< 0.05
ISO_{TRK}	$< 2.0 + 0.001p_T$
ISO_{ECAL}	$< 4.2 + 0.006p_T$
ISO_{HCAL}	$< 2.2 + 0.0025p_T$

4.5 Properties of Isolated Photons

After applying identification and isolation cuts, we end up with isolated photons. In this section some plots of the isolated photons, used in this analysis, are presented.

4.5.1 Efficiency of Photon Identification

The efficiency and its error are calculated as in Equations 4.5 and 4.6, respectively.

$$\epsilon = \frac{\sum_i w_i P_i}{\sum_i w_i (P_i + F_i)} \quad (4.5)$$

$$\delta\epsilon = \frac{\sqrt{\sum_i w_i^2 (P_i(1 - \epsilon)^2 + F_i\epsilon^2)}}{P_i + F_i} \quad (4.6)$$

where the summation runs over the Monte Carlo samples, w_i refers to the weight (cross-section / total number of events) of i^{th} sample. P , and F correspond to number of events that pass and failed the selection, respectively. Photon identification efficiency using the Monte Carlo samples indicated in Table 4.2 and Table 4.3 can be found in Figure 4.3 and in Table 4.8.

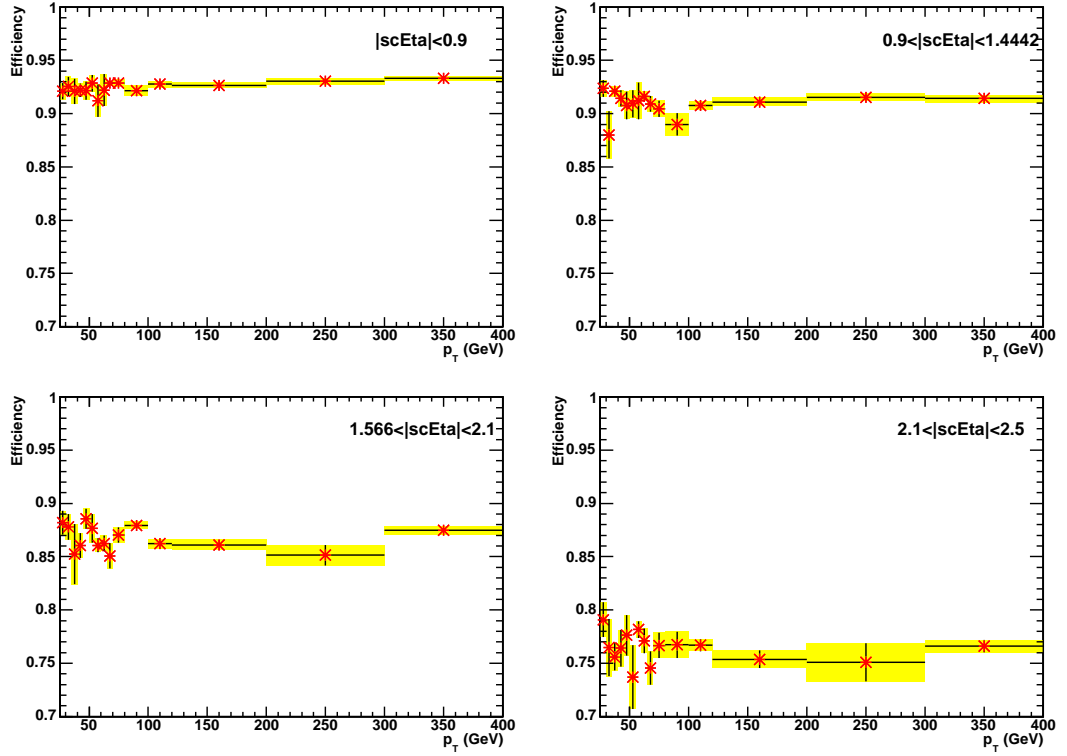


Figure 4.3: Efficiency of photon identification for each pseudo-rapidity region.

Table 4.8: Efficiency of photon identification.

Eta region	Efficiency	Efficiency Error
$ \eta_{SC} < 0.9$	0.922	0.012
$0.9 < \eta_{SC} < 1.4442$	0.909	0.019
$1.566 < \eta_{SC} < 2.1$	0.867	0.020
$2.1 < \eta_{SC} < 2.5$	0.774	0.029
Total	0.883	0.009

4.5.2 Shower Shapes of Isolated Photons

Shower shapes (shower moments) is an elegant way of looking for double peak structures. Shower shapes, $\sigma_{i\alpha i\beta}$, describes the spatial extension of the energy deposits of the shower in $\eta - \phi$ space. The $\sigma_{i\alpha i\beta}$ is calculated as follows:

$$\sigma_{i\alpha i\beta} = \sqrt{\frac{\sum_{i=1}^N (\alpha_i - \bar{\alpha})^2 (\beta_i - \bar{\beta})^2 \omega_i}{\sum_{i=1}^N \omega_i}}, \quad \omega_i = \max\left(0, 4.7 + \log \frac{E_i}{E_{5 \times 5}}\right) \quad (4.7)$$

here the summation runs over all the crystals in the electromagnetic cluster. The $(\bar{\alpha}, \bar{\beta})$ indicates the position of the super-cluster. The (α_i, β_i) and E_i refers to the position and energy of the i^{th} crystal entering the sum, respectively. Using the equation 4.7, one can easily get the equations of the variables: $\sigma_{i\eta i\eta}$, $\sigma_{i\eta i\phi}$, and $\sigma_{i\phi i\phi}$ [20, 26].

The distribution of the super-cluster eta, η_{SC} , super-cluster phi, ϕ_{SC} , and the shower shape variables $\sigma_{i\eta i\eta}$, $\sigma_{i\phi i\phi}$ are shown in the Figures 4.4, 4.5, 4.6, and 4.7.

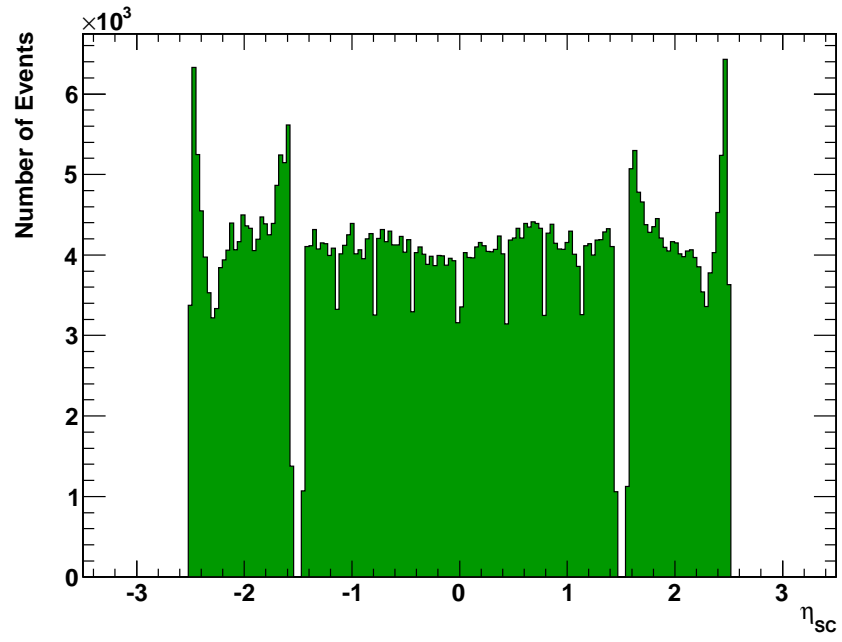


Figure 4.4: Super-cluster eta, η_{SC} , distribution of isolated photons.

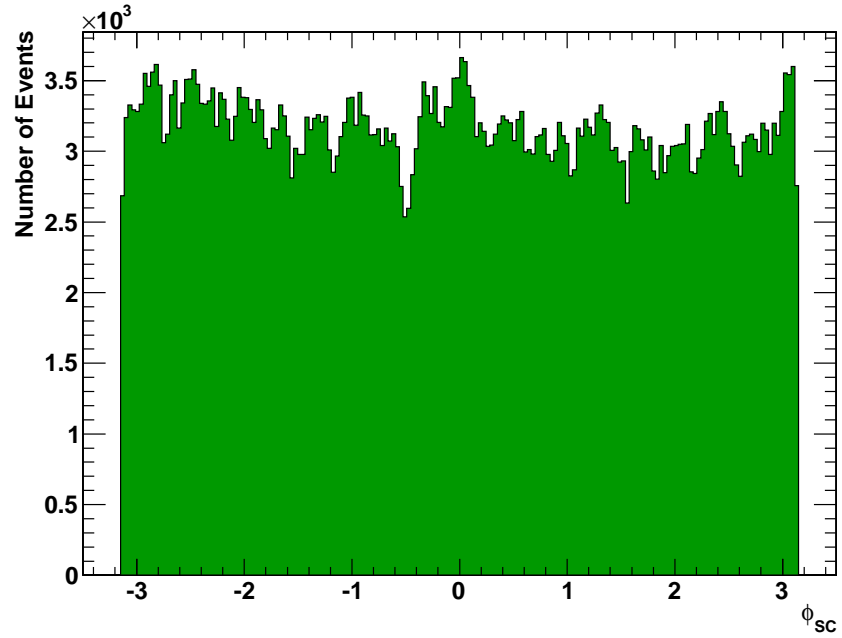


Figure 4.5: Super-cluster phi, ϕ_{SC} , distribution of isolated photons.

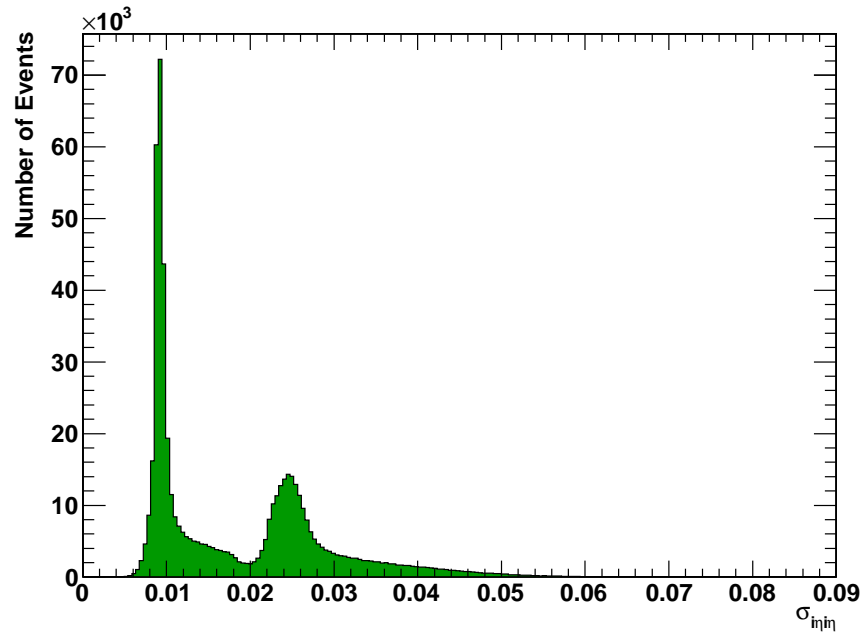


Figure 4.6: Distribution of the shower shape variable $\sigma_{\eta\eta}$ of the isolated photons.

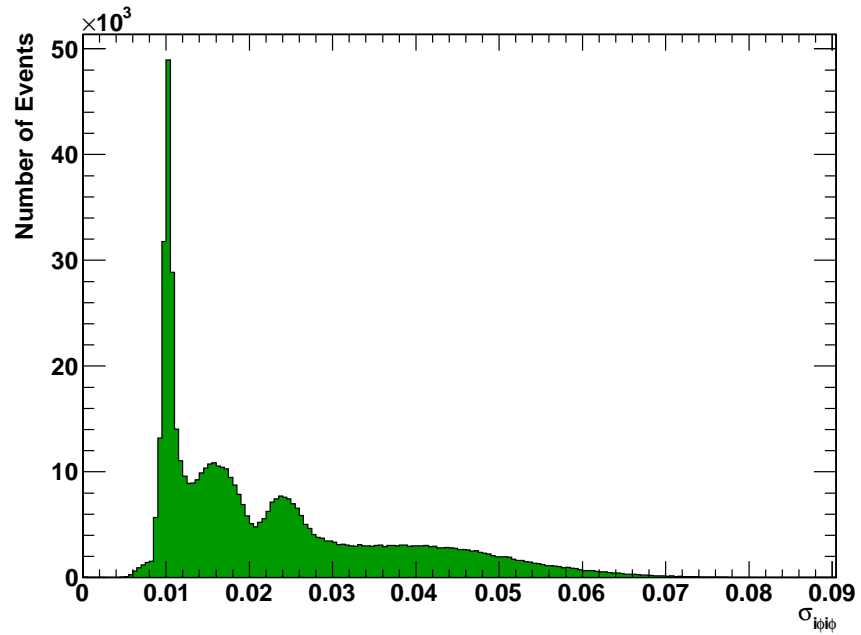


Figure 4.7: Distribution of the shower shape variable $\sigma_{\phi\phi}$ of the isolated photons.

4.6 Beam Halo Photons Removal

One of the major backgrounds to the analysis with photons is beam halo. Beam halo refers to a cloud of secondary particles, consist of muons, mesons and baryons, traveling along with the beam bunches. These secondary particles come from interactions of beam protons with the beam pipe walls or with the gas in it. Since muons are the long-lived ones of these halo particles, only they are able to traverse throughout the detector.

The halo muons that penetrate through the layers of end cap return yoke and muon subdetectors, can then undergo bremsstrahlung in the electromagnetic calorimeter. Such an effect could cause isolated clusters of energy that mimic isolated photon originating at the interaction point. It is important to study this contamination since it is a background for searches of new physics that involves photons at the final state [27].

4.6.1 Properties of Beam Halo Photons

Since the beam halo muons come from the z-direction and the endcap region of ECAL is thin in this direction, the possibility of these muons to undergo bremsstrahlung is low. So it is unlikely to have a beam halo photons in the endcap region. From the figure 4.8, it can be seen that beam halo photons mostly shows up in the barrel region. Also, as it can be seen from Figure 4.9, beam halo events in 2010 data are seen in high p_T regions. Some of the reasons that this may be caused of lack in beam quality and/or increase in luminosity.

Beam halo photons crosses the electromagnetic calorimeter in time with the brunches, however; signal photons have to transverse an extra distance from interaction point to the calorimeter. Because of this beam halo photons typically have negative timing in ECAL with respect to signal events. Figure 4.10 shows the expected arrival time of photons [28]. The arrival time of isolated photons is shown in Figure 4.11.

Shower shapes of beam halo photons are quite different from the photons coming from an interaction. Since the halo photons are coming from the z-direction they have higher $\sigma_{i\eta i\eta}$ and lower $\sigma_{i\phi i\phi}$ values. Also $\sigma_{i\eta i\eta}/\sigma_{i\phi i\phi}$ value should be higher for beam halo photons compared to signal photons. The relations between the shower shape and timing variables are shown in the following plots.

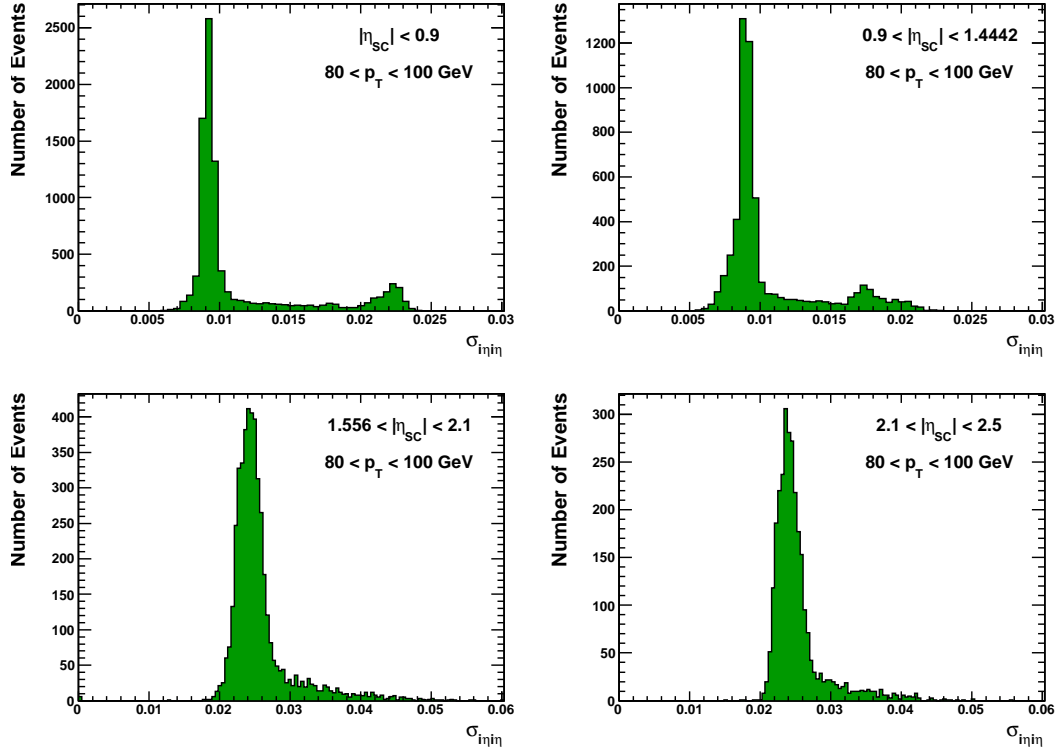


Figure 4.8: Shower shape in η -direction.

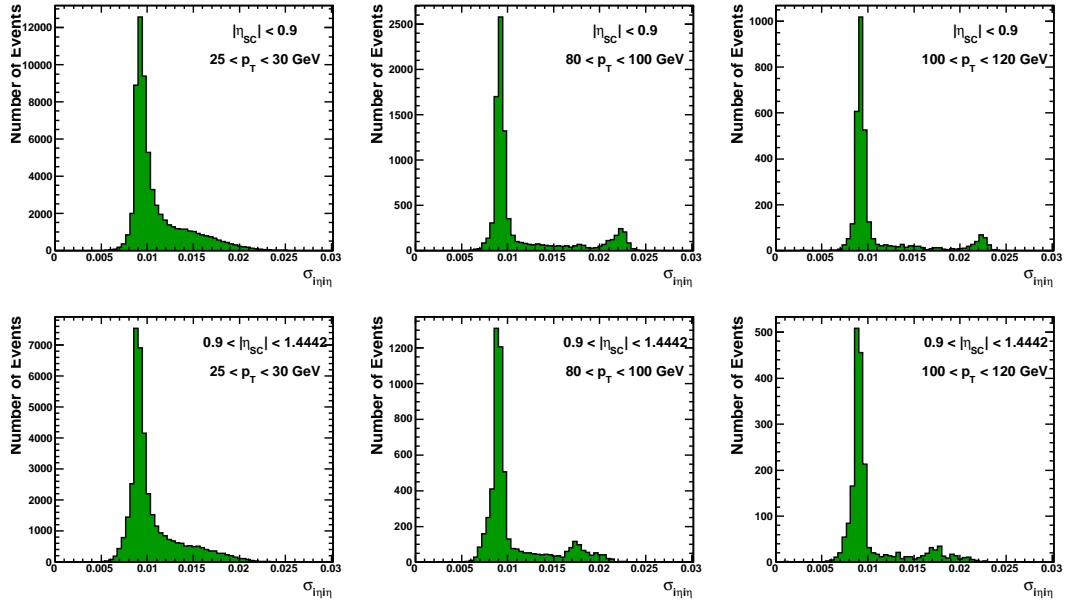


Figure 4.9: Shower shape in different p_T bins.

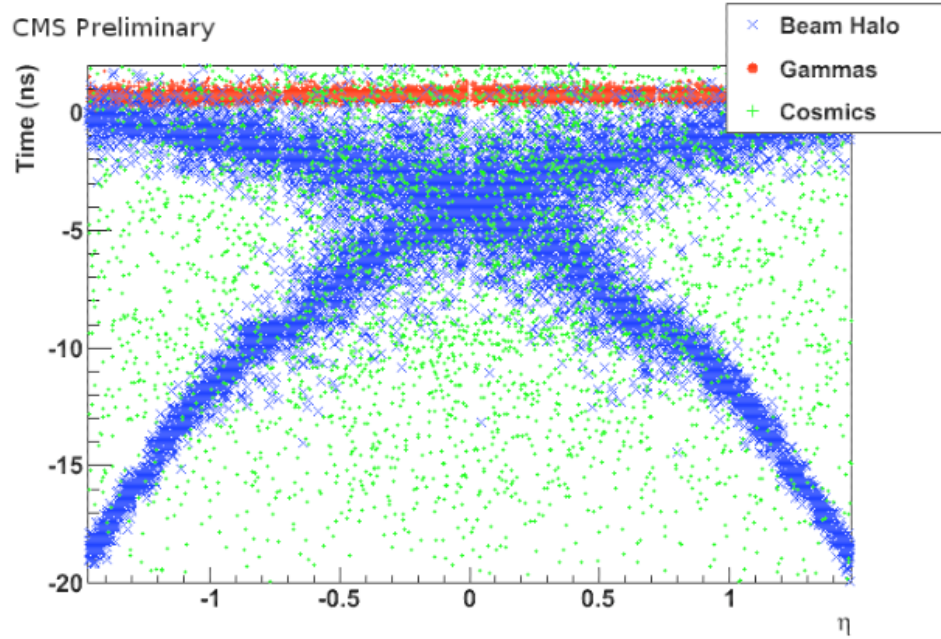


Figure 4.10: Expected arrival time of photons.

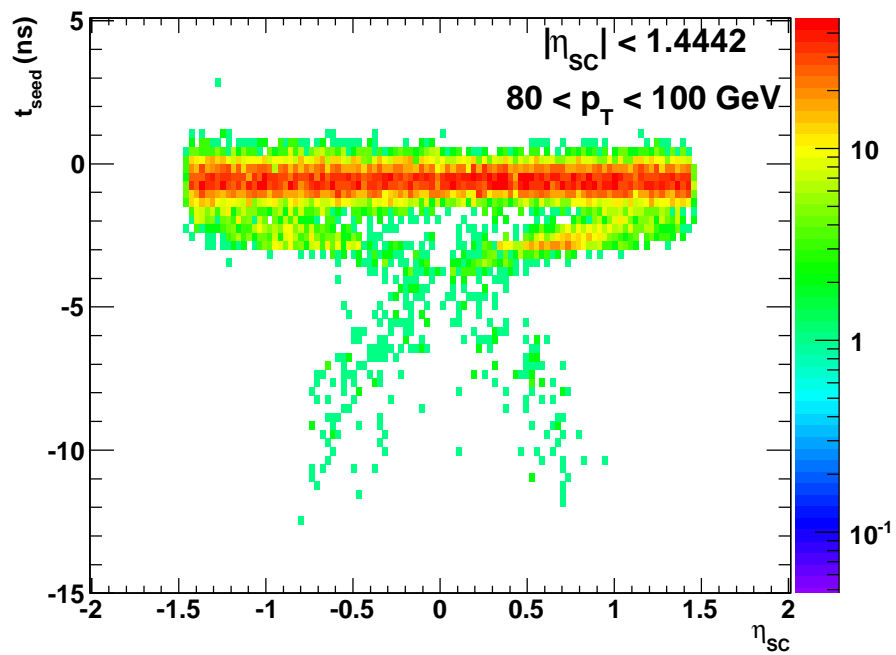


Figure 4.11: Expected arrival time of photons that have $80 < p_T < 100 \text{ GeV}$.

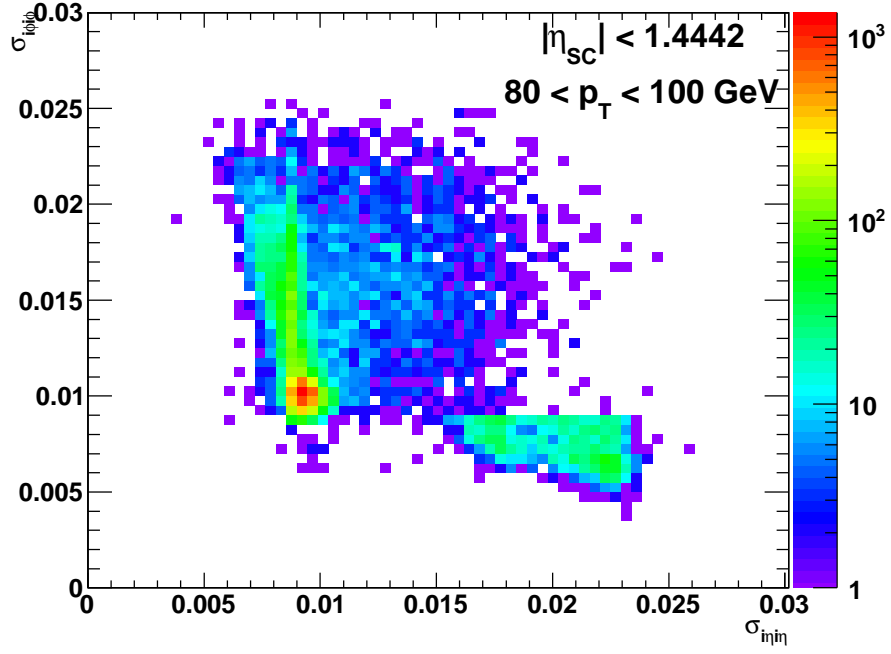


Figure 4.12: $\sigma_{i\phi\phi}$ versus $\sigma_{i\eta\eta}$ for photons that have $80 < p_T < 100$ GeV and $|\eta_{SC}| < 1.4442$.

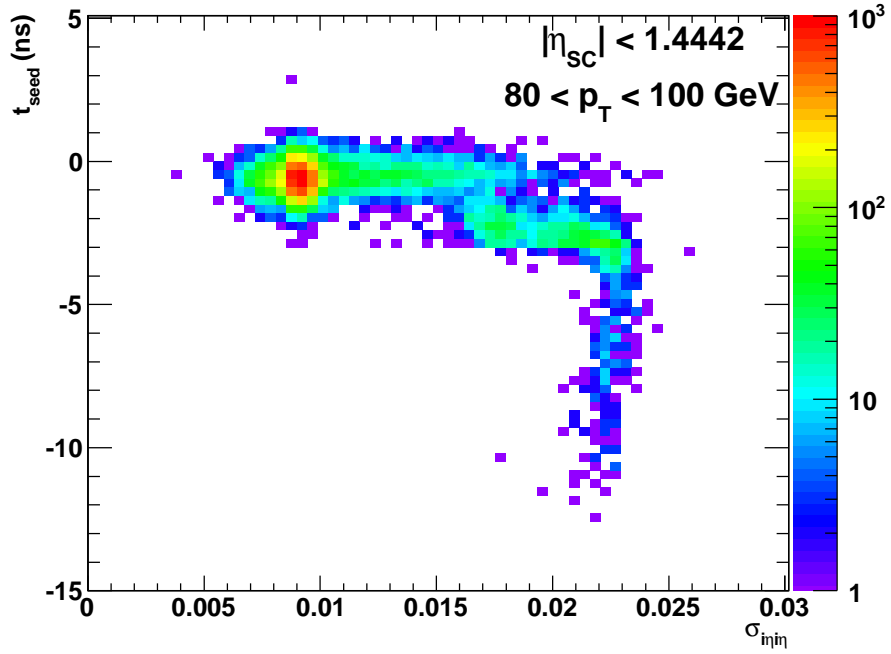


Figure 4.13: t_{seed} versus $\sigma_{i\eta\eta}$ for photons that have $80 < p_T < 100$ GeV and $|\eta_{SC}| < 1.4442$.

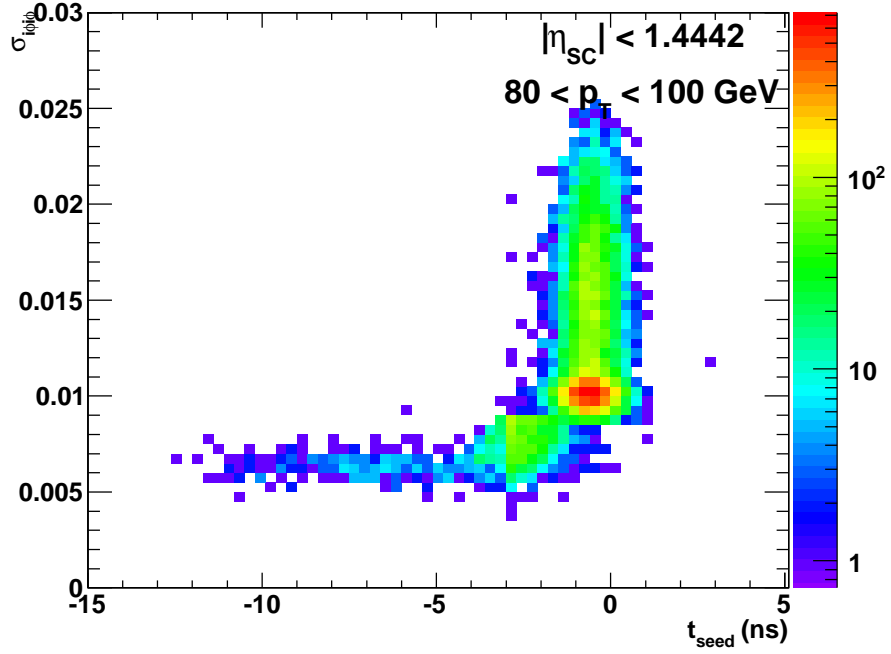


Figure 4.14: $\sigma_{i\phi i\phi}$ versus t_{seed} for photons that have $80 < p_T < 100$ GeV and $|\eta_{SC}| < 1.4442$.

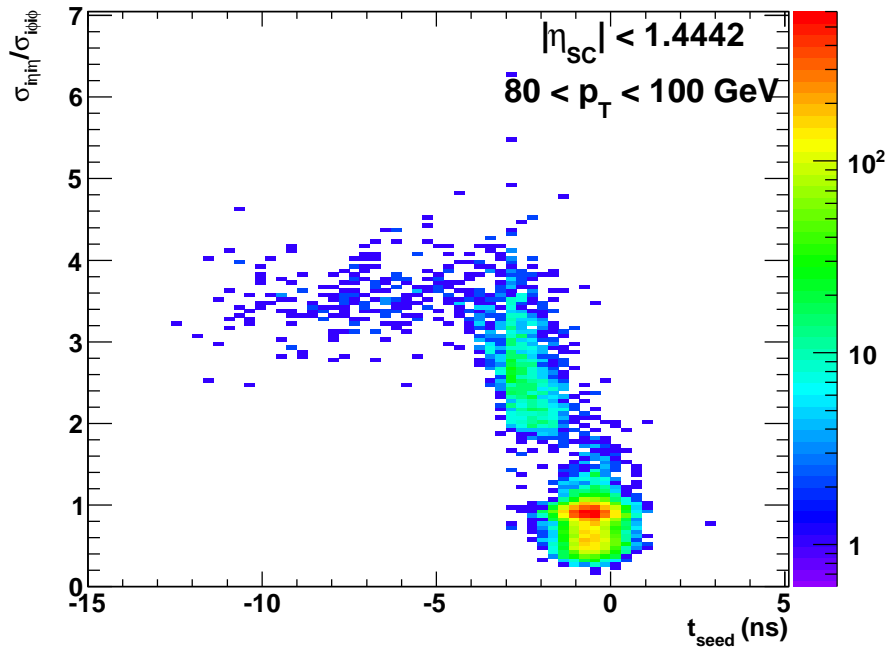


Figure 4.15: $\sigma_{i\eta i\eta} / \sigma_{i\phi i\phi}$ versus t_{seed} for photons that have $80 < p_T < 100$ GeV and $|\eta_{SC}| < 1.4442$.

4.6.2 Cuts

In this section cuts that are used to remove beam halo photons are described. Using the Figures 4.11, 4.12, 4.13 and 4.14 four different cuts are found to remove beam halo photons. Those cuts are listed in Table 4.9 and are shown in Figures 4.16, 4.17, 4.18, 4.19 and 4.20.

Table 4.9: Table of cuts that are used to remove beam halo photons.

Cut name	Condition
Timing cut	$ t_{seed} < 1.5$ ns
$\sigma_{i\phi i\phi}$ cut	$\sigma_{i\phi i\phi} > 0.009$
Rectangle cut	$\sigma_{i\phi i\phi} > 0.009$ OR $t_{seed} > -1.5$ ns
Line cut	$0.005t_{seed} + 5.21\sigma_{i\phi i\phi} - 0.039 = 0$

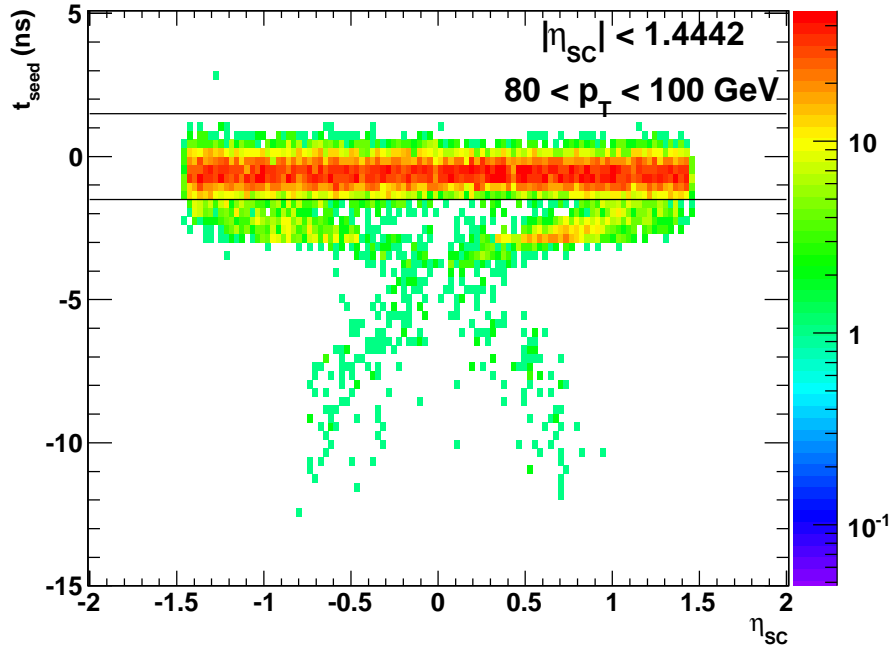


Figure 4.16: Timing cut on t_{seed} vs η_{SC} graph.

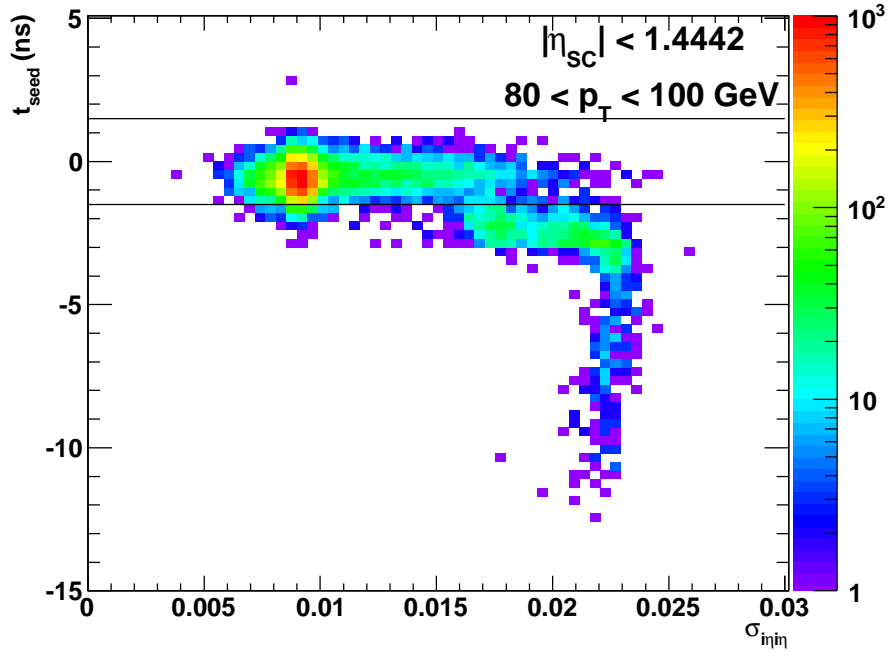


Figure 4.17: Timing cut on t_{seed} versus $\sigma_{i\eta i\eta}$ graph.

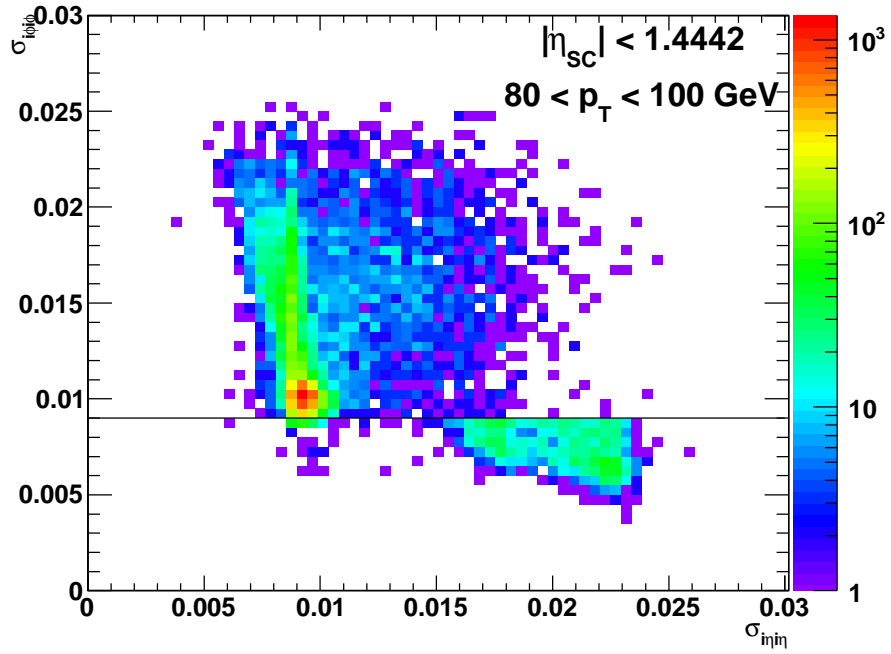


Figure 4.18: $\sigma_{i\phi i\phi}$ cut on $\sigma_{i\phi i\phi}$ versus $\sigma_{i\eta i\eta}$ graph.

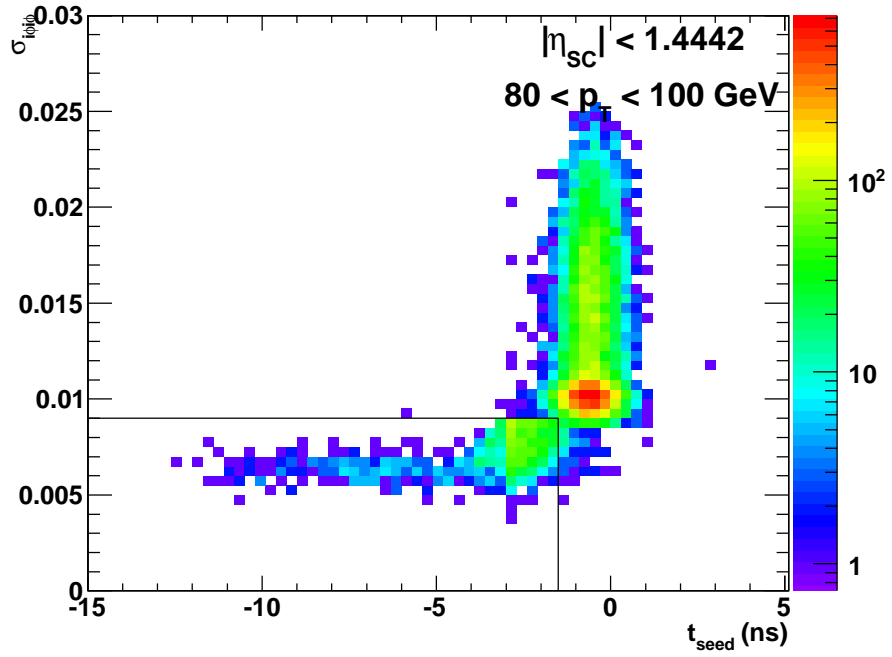


Figure 4.19: Rectangle cut on $\sigma_{ii\phi}$ versus t_{seed} graph.

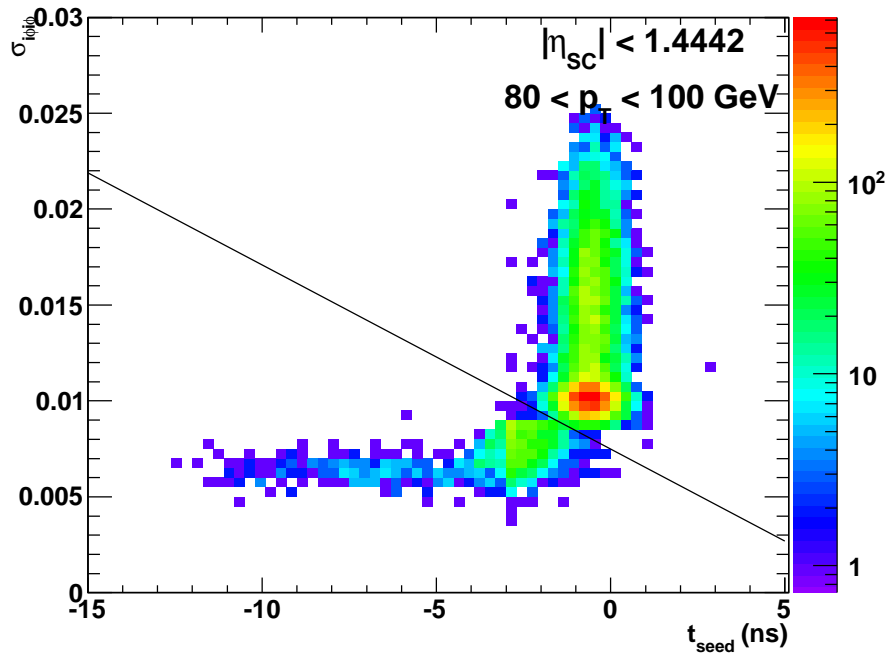


Figure 4.20: Line cut on $\sigma_{ii\phi}$ versus t_{seed} graph.

Figures 4.21, 4.22, 4.23 and 4.24 show the plots, used to estimate cuts, after each cut applied.

The $\sigma_{in\eta}$ distributions after applying the cuts are shown in Figure 4.25.

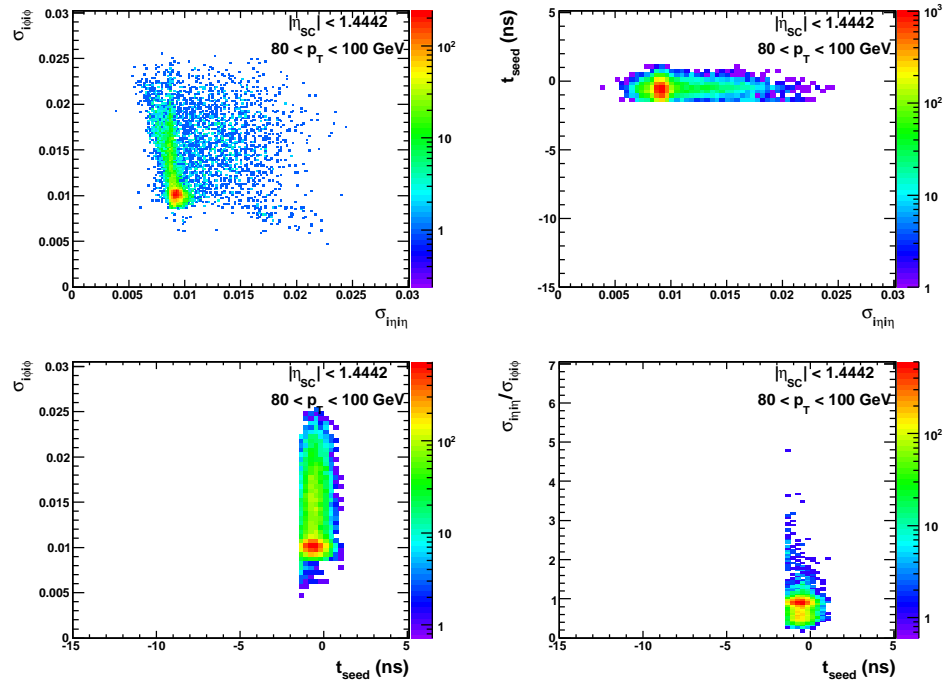


Figure 4.21: Plots after applying the timing cut.

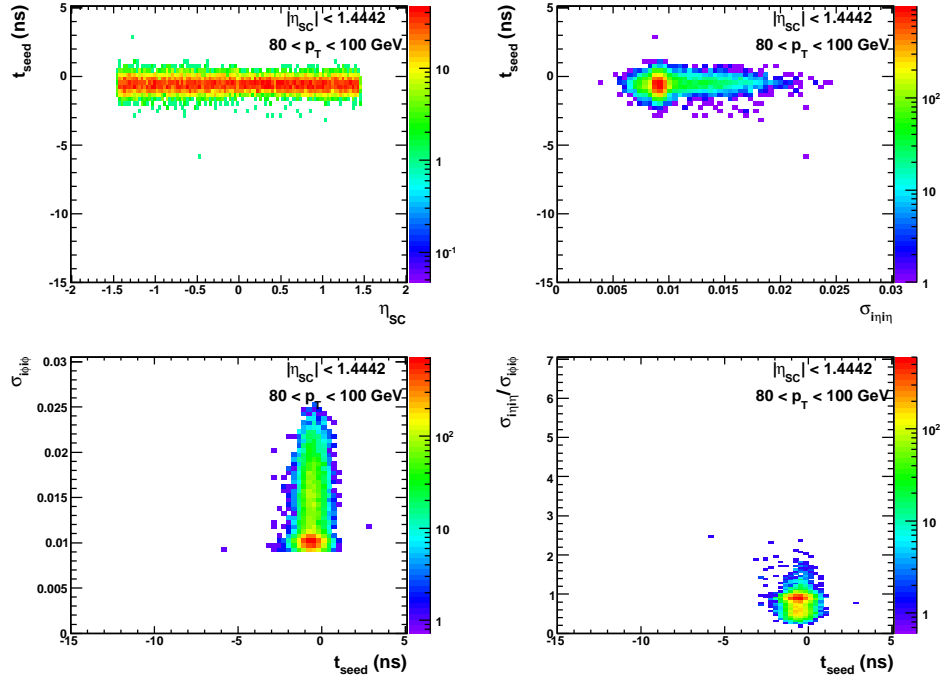


Figure 4.22: Plots after applying the $\sigma_{\phi_i\phi}$ cut.

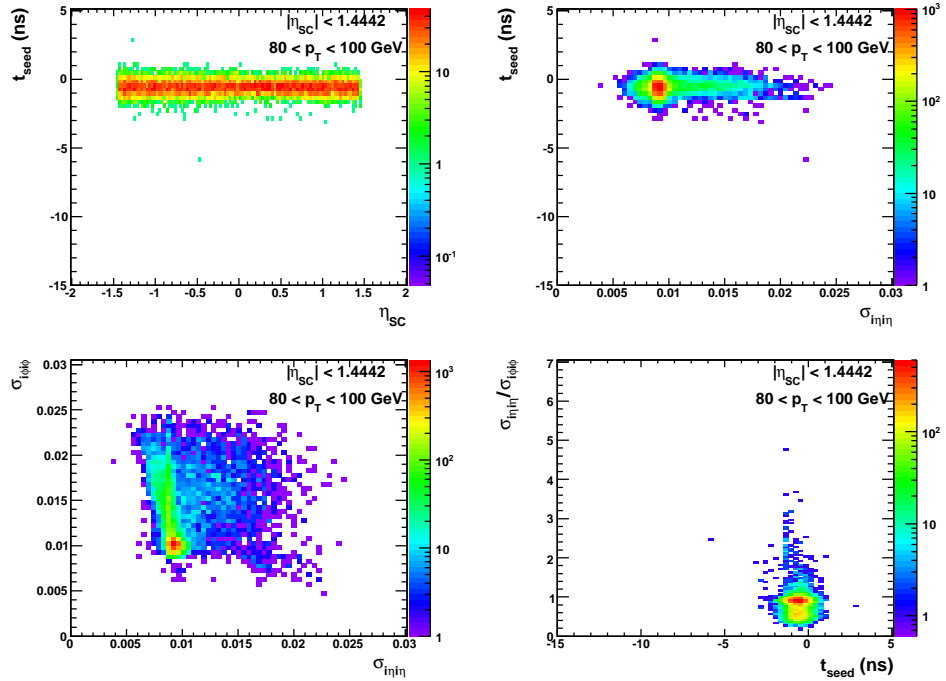


Figure 4.23: Plots after applying the rectangle cut.

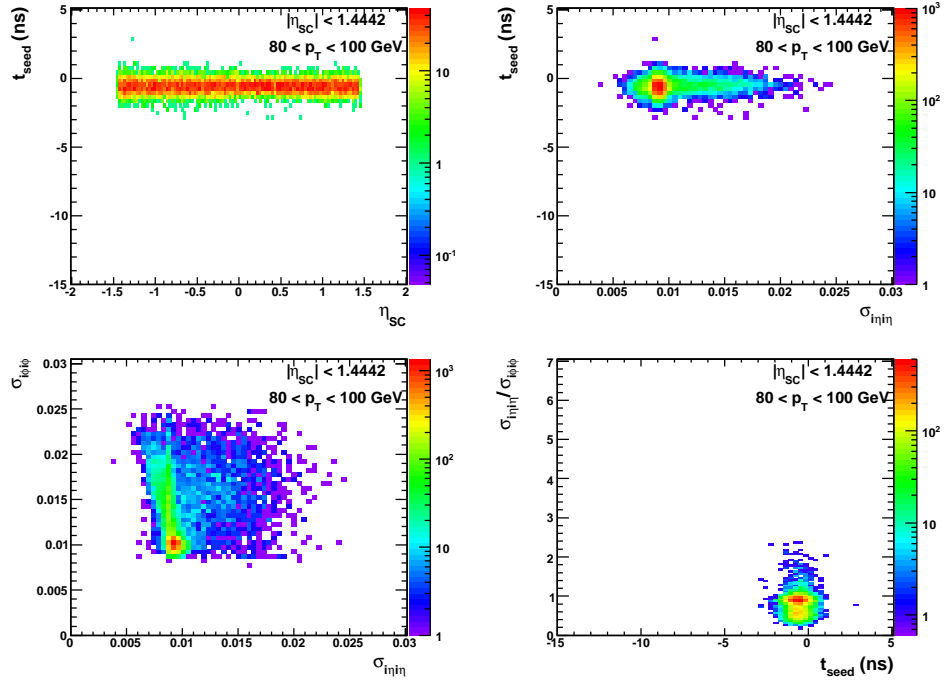


Figure 4.24: Plots after applying the line cut.

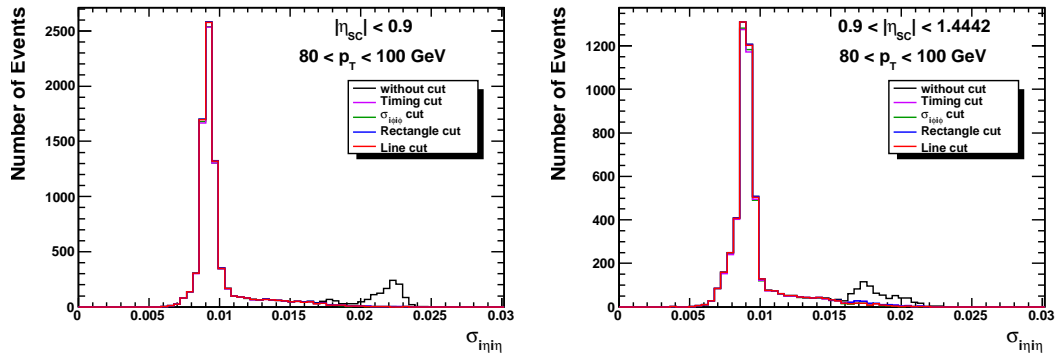


Figure 4.25: σ_{inj} distributions after applying the cuts.

4.6.3 Efficiency of the Cuts

Efficiencies of each cut are calculated as described in sub-section 4.5.1 using the samples summarized in Tables 4.2 and 4.3. The efficiencies and their errors, calculated for each p_T bin, for each cut are shown in Figures 4.26, 4.27, 4.28 and 4.29. The overall efficiencies and their errors are also calculated for each pseudo-rapidity region: central barrel ($0 < |\eta_{SC}| < 0.9$), outer barrel ($0.9 < |\eta_{SC}| < 1.4442$) as well as for overall barrel region ($|\eta_{SC}| < 1.4442$). The efficiencies for these regions are summarized in Tables 4.10, 4.11, 4.12 and 4.13.

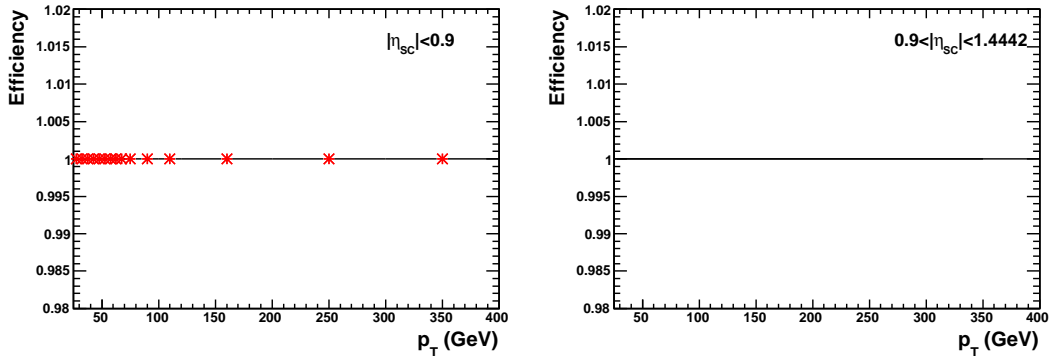


Figure 4.26: Efficiency for the timing cut.

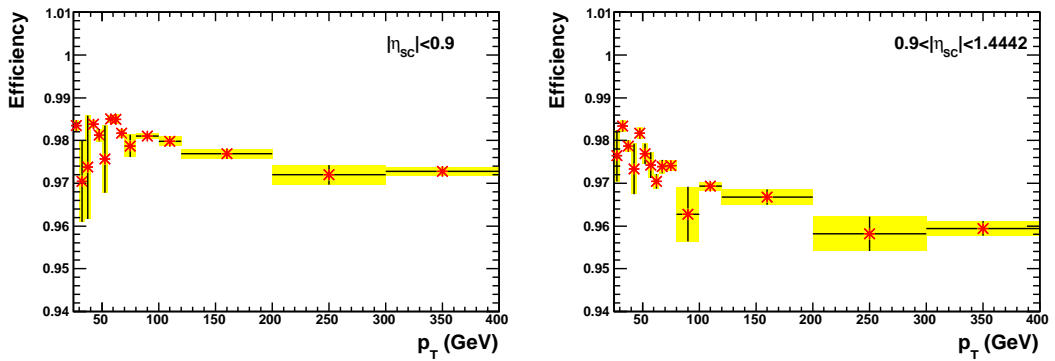


Figure 4.27: Efficiency for the $\sigma_{i\phi_i\phi}$ cut.

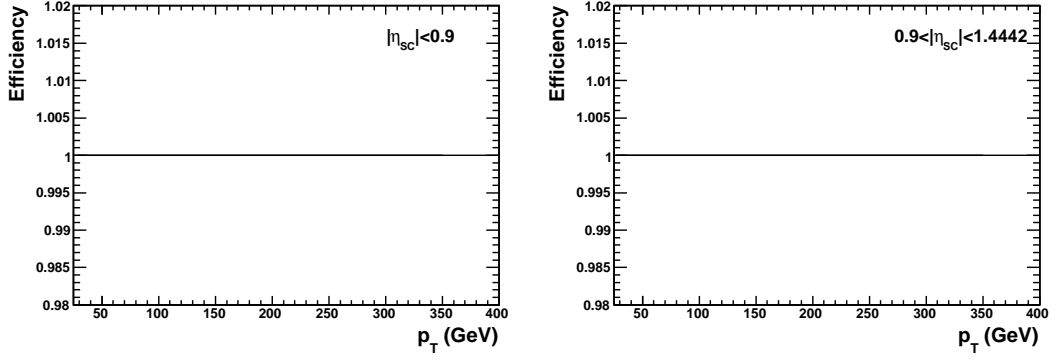


Figure 4.28: Efficiency for the rectangle cut.

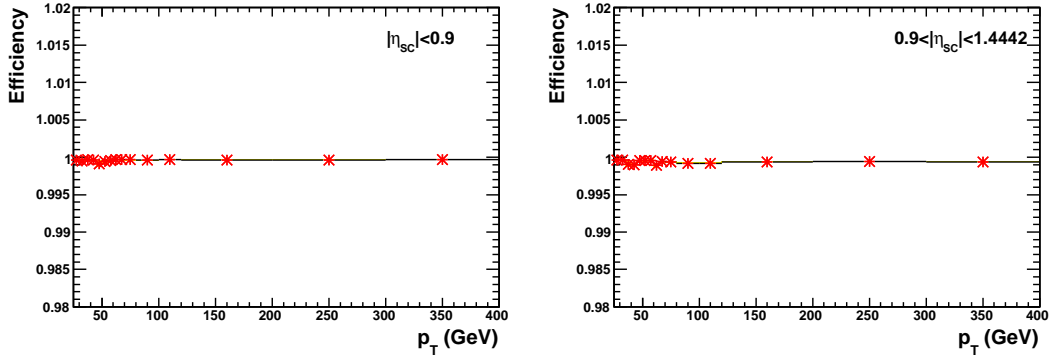


Figure 4.29: Efficiency for the line cut.

Table 4.10: Efficiency of the timing cut.

Eta region	Efficiency	Error of Efficiency
Central barrel	1	5.89×10^{-6}
Outer barrel	1	0
Overall barrel	1	2.35×10^{-6}

Table 4.11: Efficiency of the $\sigma_{i\phi}$ cut.

Eta region	Efficiency	Error of Efficiency
Central barrel	0.979	0.008
Outer barrel	0.978	0.008
Overall barrel	0.986	0.004

Table 4.12: Efficiency of the rectangle cut.

Eta region	Efficiency	Error of Efficiency
Central barrel	1	0
Outer barrel	1	0
Overall barrel	1	0

Table 4.13: Efficiency of the line cut.

Eta region	Efficiency	Error of Efficiency
Central barrel	1	2.21×10^{-4}
Outer barrel	0.999	2.76×10^{-4}
Overall barrel	1	1.10×10^{-4}

CHAPTER 5

CONCLUSION

The photon measurements in the CMS experiment are important because of many reasons discussed in both Chapter 1 and Chapter 4. In order to achieve precise measurement of the photon cross sections, the background studies are crucial as well as the identification and isolation selections. The identification and isolation selections applied to the data are presented in Chapter 4. It is seen that some background photons still survive after these selections are applied. The main subject of this thesis is to study this background contamination coming from the beam halo events. The shower shape and timing characteristics of the photons, that are coming from the beam halo events, are presented and four different cuts are developed according to these characteristics in order to remove the contamination.

The cuts that are used to remove beam halo photons are presented in Chapter 4. After the cuts applied, the plots of the variables, that are used to identify beam halo photons, are shown in Figures 4.21, 4.22, 4.23 and 4.24. Also, the efficiencies of the cuts that are obtained using the Monte Carlo samples are summarized in Tables 4.10, 4.11, 4.12 and 4.13. As it can be seen from the Figure 4.25, each cut removes beam halo photons efficiently. However; each cut has advantages and disadvantages. Further analysis of the cuts using these information is discussed below:

- **Timing cut:** From the plot of the $\sigma_{i\phi i\phi}$ vs. $\sigma_{i\eta i\eta}$ in Figure 4.21, it can be said that there are some beam halo photons remaining after the timing cut. And by looking at the other plots in Figure 4.21, it is seen that the timing cut removes some signal photons, although it has 100% efficiency.
- **$\sigma_{i\phi i\phi}$ cut:** From the plots in Figure 4.22, it is seen that a negligible amount of beam

halo photons are remained after applying this cut. However; from the plot of the $\sigma_{i\phi i\phi}$ vs. t_{seed} in Figure 4.22, it can be said that this cut removes some of the signal photons, too. Also this cut has the lowest efficiency.

- **Rectangle cut:** By looking at the plots of the $\sigma_{i\phi i\phi}$ vs. $\sigma_{i\eta i\eta}$ and the $\sigma_{i\eta i\eta}/\sigma_{i\phi i\phi}$ vs. t_{seed} in Figure 4.23, it is seen that this cut can not remove all of the beam halo photons. The advantage of this cut is that it does not cut signal photons and it has 100% efficiency.
- **Line cut:** By looking at the all plots in Figure 4.24, it can be inferred that this cut removes all the beam halo photons while keeping the all signal photons. Moreover, its efficiency is 100%.

Considering the advantages and the disadvantages of the cuts discussed above, the line cut seems to be the most advantageous cut. However; the efficiencies used in this analysis are calculated using the Monte Carlo simulations which have limited precision. In order to get more precise efficiency results one may use the data driven techniques [29].

The results of this analysis, which is also presented in the CMS internal notes [11], may be used to check the beam halo contamination in the data that will be taken by CMS in the future as well as in the cross section measurements of photon production in the CMS experiment.

REFERENCES

- [1] D. Griffiths. *Introduction to Elementary Particles*. WILEY-VCH, 2nd edition, 2008.
- [2] D. H. Perkins. *Introduction to High Energy Physics*. Cambridge University Press, 4th edition, 2000.
- [3] Fayyazuddin and Riazuddin. *A Modern Introduction to Particle Physics*. World Scientific, 2nd edition, 2000.
- [4] K. Gottfried and V. F. Weisskopf. *Concepts of Particle Physics*, volume II. Oxford University Press, 1986.
- [5] CMS Collaboration. Measurement of the isolated prompt photon production cross section in pp collisions at $\sqrt{s} = 7$ TeV. *Phys. Rev. Lett.*, 106, 2011.
- [6] ATLAS Collaboration. Measurement of the inclusive isolated prompt photon cross section in pp collisions at $\sqrt{s} = 7$ TeV with the ATLAS detector. *Phys. Rev. D*, 83, 2011.
- [7] L. Evans and P. Bryant. LHC machine. *JINST*, 3(S08001), 2008.
- [8] CMS Collaboration. The CMS experiment at the CERN LHC. *JINST*, 3(S08004), 2008.
- [9] CMS Collaboration. *CMS Physics Technical Design Report Volume I: Detector Performance and Software*. CERN, Geneva, 2006.
- [10] CMS Collaboration. *CMS The TriDAS Project Technical Design Report, Volume 2: Data Acquisition and High-Level Trigger*. CERN, December 2002.
- [11] CMS Collaboration. Beam halo removal with shower shape template in 2010 data. CMS Note AN-11-336, 2011.
- [12] Particle data group. <http://pdg.lbl.gov/>. Last accessed on 14/09/2011.
- [13] CERN public web-site. <http://public.web.cern.ch/public/en/LHC/LHC-en.html>. Last accessed on 05/07/2011.
- [14] J. Allday. *Quarks, Leptons and the Big Bang*. Taylor & Francis, 2nd edition, 2002.
- [15] V. D. Barger and R. J. N. Phillips. *Collider Physics*. Frontiers in Physics Lecture Note Series. Addison-Wesley, 1987.
- [16] M. Veltman. *Facts and Mysteries in Elementary Particle Physics*. World Scientific, 2003.
- [17] Taking a closer look at LHC. <http://www.lhc-closer.es>. Last accessed on 05/07/2011.
- [18] CMS public web-site. <http://cms.web.cern.ch/cms/index.html>. Last accessed on 05/07/2011.

- [19] CMS Collaboration. Measurement of isolated photon production cross section in pp collisions at $\sqrt{s} = 7$ TeV. CMS Note AN-10-268, 2010.
- [20] CMS Collaboration. Measurement of the differential isolated prompt photon production cross section in pp collisions at $\sqrt{s} = 7$ TeV. CMS Note QCD-10-037, 2011.
- [21] CMS Collaboration. Measurement of isolated photon production cross section in pp collisions at $\sqrt{s} = 7$ TeV with isolation template and 2010 dataset. CMS Note AN-11-066, 2011.
- [22] J. Pumplin et al. New generation of parton distributions with uncertainties from global QCD analysis. *JHEP*, 07, 2002.
- [23] CMS Collaboration. Photon reconstruction and identification at $\sqrt{s} = 7$ TeV. CMS EGM-10-005, 2010.
- [24] CMS Collaboration. Electron reconstruction in the CMS electromagnetic calorimeter. CMS Note 2001/034, 2001.
- [25] CMS Collaboration. Review of clustering algorithms and energy corrections in ECAL. CMS IN-2010/008, 2010.
- [26] P. Musella. *Measurement of the inclusive photon production cross section and study of associated W -photon production in proton-proton collisions at the LHC*. PhD thesis, Technical University of Lisbon, 2010.
- [27] CMS Collaboration. Data-driven determination of beam halo contamination in photon candidates. CMS AN 2010/115, 2010.
- [28] P. Zalewski. Search for standard and exotic supersymmetry signatures at CMS. *Acta. Phys. Pol. B*, 41(7), 2010.
- [29] CMS Collaboration. Photon efficiency measurements using tag and probe. CMS Note AN-10-292, 2010.